Report of AAPM Therapy Physics Committee Task Group 74: In-air output ratio, S_c, for megavoltage photon beams

Timothy C. Zhu[a)]
University of Pennsylvania, Philadelphia, Pennsylvania 19104

Anders Ahnesjö
Uppsala University, 751 85 Uppsala, Sweden and Nucletron AB, Box 1704, 751 47 Uppsala, Sweden

Kwok Leung Lam
University of Michigan, Ann Arbor, Michigan 48109

X. Allen Li
Medical College of Wisconsin, Milwaukee, Wisconsin 53226

Chang-Ming Charlie Ma
Fox Chase Cancer Center, Philadelphia, Pennsylvania 19111

Jatinder R. Palta
University of Florida, Gainesville, Florida 32610

Michael B. Sharpe
Princess Margaret Hospital, Toronto, ON M5G 2M9, Canada

Bruce Thomadsen
University of Wisconsin, Madison, Wisconsin 53705

Ramesh C. Tailor
RPC, UT MD Anderson Cancer Center, Houston, Texas 77030

(Received 1 September 2008; revised 21 August 2009; accepted for publication 21 August 2009; published 20 October 2009)

The concept of in-air output ratio (S_c) was introduced to characterize how the incident photon fluence per monitor unit (or unit time for a Co-60 unit) varies with collimator settings. However, there has been much confusion regarding the measurement technique to be used that has prevented the accurate and consistent determination of S_c. The main thrust of the report is to devise a theoretical and measurement formalism that ensures interinstitutional consistency of S_c. The in-air output ratio, S_c, is defined as the ratio of primary collision water kerma in free-space, K_p, per monitor unit between an arbitrary collimator setting and the reference collimator setting at the same location. Miniphantoms with sufficient lateral and longitudinal thicknesses to eliminate electron contamination and maintain transient electron equilibrium are recommended for the measurement of S_c. The authors present a correction formalism to extrapolate the correct S_c from the measured values using high-Z miniphantom. Miniphantoms made of high-Z material are used to measure S_c for small fields (e.g., IMRT or stereotactic radiosurgery). This report presents a review of the components of S_c, including headscatter, source-obscuring, and monitor-backscattering effects. A review of calculation methods (Monte Carlo and empirical) used to calculate S_c for arbitrary shaped fields is presented. The authors discussed the use of S_c in photon dose calculation algorithms, in particular, monitor unit calculation. Finally, a summary of S_c data (from RPC and other institutions) is included for QA purposes. © *2009 American Association of Physicists in Medicine.*
[DOI: 10.1118/1.3227367]

Key words: in air output ratio, headscatter, output factor, energy fluence, miniphantom, megavoltage photon, extra focal source, MU calculation

TABLE OF CONTENTS

LIST OF SYMBOLS

The symbols used for all physical quantities in the report are listed here. Arguments to the dosimetry quantities are grouped such that those dependent on the radiation field geometry (e.g., c or A), the position relative to the radiation source (x,y,z), and the phantom geometry specifications (e.g., d, and SSD) are placed together where the groups are separated by a semicolon. The group always follow the same order, e.g., $D(c,s;x,y,z;d,\mathrm{SSD})$. Whenever we emphasize selected variables, we will ignore the other variables, e.g., $D(x,y,z)$. When the energy fluence Ψ is required as an explicit variable, it will be placed as the last group, e.g., $D(x,y,z;\Psi(A;x,y,z_{\mathrm{ref}}))$.

β = Dose to collision kerma ratio (unitless) [see Eq. (11)]
ε = Electron disequilibrium factor (unitless) [see Eq. (13)]
ω = Dose-to-energy fluence ratio (unit: $\mathrm{cm^2\,g^{-1}}$) [see Eq. (23)]
λ = width of indirect radiation source at isocenter (unit: cm) [see Eq. (36)]
Ψ = Photon energy fluence (unit: $\mathrm{MeV\,cm^{-2}}$) [see Eq. (23)]
Ψ_E = Photon energy fluence differential in photon energy E (unit: $\mathrm{cm^{-2}}$) [see Eq. (6)]
Ψ_0 = Photon energy fluence of direct particles at isocenter (unit: $\mathrm{MeV\,cm^{-2}}$) [see Eq. (23)]
Ψ_{ind} = Photon energy fluence of indirect photons, also called headscatter photons (unit: $\mathrm{MeV\,cm^{-2}}$) [see Eq. (26)]
μ_{en}/ρ = Mass energy absorption coefficient (unit: $\mathrm{cm^2\,g^{-1}}$) [see Eq. (6)]
μ = linear attenuation coefficient (unit: $\mathrm{cm^{-1}}$) [see Eq. (6)]
A = Aperture setting, refer to a particular state of settings for all collimation (a function of c and s) [see Eq. (23)]
A_{ref} = Aperture setting for the reference (or normalization) field [see Eq. (27)]
$\hat{A}$ = Irradiated backscattering area of aperture A [see Eq. (29)]
a_1 = Fitting parameter for monitor-backscattering effect, also called monitor-backscattering coefficient (unit: $\mathrm{cm^{-1}}$) [see Eq. (36)]
a_2 = Fitting parameter for in-air output ratio for total headscatter as a percentage of direct radiation (unitless) [see Eq. (36)]
B = Beam modifiers (e.g., wedges, trays) [see Eq. (7)]
b = Backscatter signal fraction (unitless) [see Eq. (29)]
c = Collimator setting, usually referring to the side of the equivalent square of a field and always specified at isocenter (unit: cm) [see Eq. (3)]
c_{ref} = Collimator setting for the reference (or normalization) field, also specified at the isocenter (unit: cm) [see Eq. (3)]
c_x, c_y = X- and Y- jaw collimator settings, always specified at the isocenter (unit: cm) [see Eq. (32)]
D = Absorbed dose (unit: Gy)
D_{p} = Primary dose, i.e., absorbed dose from charged particles released from the photon's first interaction in the patient (unit: Gy) [see Eq. (9)]
D_{s} = Scatter dose, i.e., absorbed dose from charged particles released from the photon's second or later interactions in the patient (unit: Gy)
DIST = The distance factor that relates kerma to distance from the source (unitless) [see Eq. (17)]
d = Depth (unit: cm)
$\overline{d}$ = Average depth (unit: cm) for scatter factor calculation [see Eq. (18)]
d_{ref} = Reference (or normalization) depth (unit: cm)
E = Photon energy (unit: MeV)
f = Relative lateral distribution of the total energy fluence (unitless) [see Eq. (26)]
H_0 = Normalization constant for S_c (unitless) [see Eq. (36)]
HCF = Headscatter correction factor, ratio of S_c between the MLC shaped field and that of the rect-

angular field encompassing the irregular field (unitless) [see text after Eq. (38)]

K = Collision kerma (K_{dir} for direct beam, K_{air} for kerma in air, K_h for headscatter component) (unit: Gy) [see Eq. (11)]

K_{inc} = Incident collision kerma, i.e., the kerma incident on the patient (unit: Gy) [see Eq. (12)]

K_p = Primary collision kerma (unit: Gy) [see Eq. (11)]

K_s = Scatter collision kerma resulting from photons generated from other interactions in the patient or phantom (unit: Gy)

k = Collimator exchange coefficient (unitless) [see Eq. (33)]

k_b = Collimator backscatter coefficient (unitless) [see Eq. (29)]

MU = Monitor unit (unit: MU) [see Eq. (2)]

MU_0 = Direct monitor signal, proportional to the fluence of direct photons (unit: MU) [see Eq. (24)]

MU_b = Backscatter monitor signal, proportional to the fluence of particles backscattered by the collimators (unit: MU) [see Eq. (24)]

$N(c_y)$ = Calculated normalization factor fraction of MU delivered to isocenter for soft wedges [e.g., Varian (enhanced) dynamic wedge] for Y-jaw setting of c_y. (unitless) [see Eq. (39)].

O_{air} = In-air output function (unitless) [see Eq. (7)]

POAR(x)= Pimary off-axis ratio at x (unitless) [see Eq. (22)]

S_c = In-air output ratio (unitless) [see Eq. (3)]

S_{cp} = (In-water) output ratio (unitless) [see Eq. (2)]

S_b = Monitor-backscatter factor (unitless) [see Eq. (27)]

$S_{c,n}$ = In-air output ratio for enhanced dynamic wedge with effect of reduced MU delivered on the central axis taken out (unitless) [see text before Eq. (39)]

$S_{c,w}$ = In-air output ratio for wedge (unitless) [see Eq. (20)]

S_h = Component of in-air output ratio due entirely to headscatter (unitless) [see Eq. (27)]

S_p = Phantom scatter factor (unitless) [see Eq. (8)]

SAD = Source-to-axial distance, usually 100 cm (unit: cm) (see Fig. 2)

SF = Dose scatter factor, equals 1 + SPR (unitless) [see Eq. (1)]

SF_K = Kerma scatter factor, similar to SF but replacing the absorbed dose with kerma (unitless) [see Eq. (11)]

SPD = Source-to-point distance, same as z (unit: cm) [see text after Eq. (17)]

SSD = Source-to-skin (or surface) distance (unit: cm) (see Fig. 2)

SDD = Source-to-detector distance, same as z (unit: cm) (see Fig. 2)

SPR = Scatter-to-primary dose ratio, D_s/D_p (unitless)

SPR_{air} = Scatter-to-primary kerma ratio between indirect and direct radiation (unitless) [see Eq. (36)]

STT = Segmented treatment table (unitless) [see Eq. (39)]

s = Projected field size at point of interest and always measured at depth (unit: cm) (see Fig. 2)

$S^{S\text{-}A}_{med,det}$ = Spencer–Attix stopping power ratio for a medium "med" to a detector cavity medium "det" (unitless) [see Eq. (30)]

s_{ref} = Projected field size at point of interest for the reference (or normalization) field (unit: cm) (see Fig. 2)

s_{SSD} = Field size at phantom or patient surface (unit: cm) (see Fig. 2)

T = Transmission function resulting from attenuation of material in the beam: A function of depth, d and A (unitless) [see Eq. (12)]

TPR = Tissue-phantom ratio (unitless) [see Eq. (13)]

X = Signal reading from a detector (unit: C) [see Eq. (6)]

x,y = Lateral positions relative to axis of collimator rotation (unit: cm) [see Eq. (5)]

z = Distance from the source to the point of interest (z_{SMD}, z_{SCD}, and z_{MCD} are the distances from source to monitor chamber, source to collimator, and monitor chamber to collimator, respectively) (unit: cm) [see Eq. (5)]

z_{MCD} = Monitor to backscattering surface distance (unit: cm)

z_{SMD} = Source to monitor distance (unit: cm) [see Fig. 1]

z_{SCD} = Distance from the source to the backscattering collimator surface (unit: cm)

z_{ref} = Reference (or normalization) distance from the source to the point of interest (unit: cm) [see Eq. (2)]

I. INTRODUCTION AND SCOPE

The concept of in-air output ratio (S_c) was introduced to characterize how the incident photon fluence per monitor unit (MU) (or unit time for a Co-60 unit) varies with collimator settings.[1–3] This quantity is also called the in-air output factor,[4] collimator-scatter factor,[5] headscatter factor,[6,7] and in common usage, the field size factor. The names, collimator-scatter factor and headscatter factor, are somewhat misleading since they emphasize a single component of the output ratio, while the last is unspecific as to which quantity that varies with the field size. We retained the symbol S_c because it has been widely used in North America.[5] The development of three-dimensional conformal radiotherapy (3D CRT) in the 1990s motivated investigation of models and experimental procedures to quantify different components of the accelerator output to provide more accurate dose computation. There are multiple factors[8] shown to influence the in-air output ratio; in particular, photons are scattered by structures in the accelerator head (headscatter), photons and electrons are

backscattered into the monitor chamber (monitor backscatter), and at very small field sizes, a portion of the x-ray source is obscured by the collimators (source-obscuring effect). Various sources of headscatter, which include the primary collimator, the flattening filter, the secondary collimators, the monitor chamber (and a wedge, if used), have been characterized. Several studies have measured the actual source distributions for the target as well as for the extended headscatter source at the flattening filter.[9–11] The availability of Monte Carlo simulation has provided a methodology to study various components of the headscatter to interpret the measurement results or validate analytical models.

Without a commonly agreed formal definition, an in-air output ratio has been widely applied in various approaches for calculation of absorbed dose per MU. These approaches include derivation of parameters for explicit modeling of headscatter components as well as for direct use in factor-based monitor unit calculation schemes. Use of asymmetric jaws has compelled the need to characterize S_c on and off the central axis. The introduction of intensity-modulated radiotherapy (IMRT) has further required S_c inside and outside beam collimation. Accurate determination of in-air output ratios for IMRT is much more challenging, where extremely small and/or severe irregularly shaped fields are being more commonly used.

The main thrust of the report is about devising a theoretical and measurement formalism that ensures interinstitutional consistency of S_c. Historically, S_c is often measured at depth of maximum dose with a build-up cap. This experimental definition of S_c, while popular for TMR-based MU calculation formalism, is fundamentally different from the in-air output ratio (S_c) as defined in this report. For clarity, we will refer to the old definition of S_c as collimator-scatter factor. Detailed discussion on the use of the collimator-scatter factor is beyond the scope of TG74 because of the large interinstitutional variations, lack of published theoretical investigations of the behavior of contaminating electrons, and other potential complications (e.g., detector response difference for electrons and photons) caused by the contaminating electrons.

There has been much confusion regarding the measurement technique to be used that has prevented the accurate and consistent determination of S_c. Ideally, the build-up cap/miniphantom should provide full electron equilibrium as in full water medium, with negligible photon scattering, and be small enough to be fully covered by a homogeneous part of the radiation beam. In this report, "full water phantom" will be referred to simply as "in water." The shape, dimension, and material of the build-up cap/miniphantom, and the type and size of the detector are all design considerations. Earlier designs of build-up caps were thin shells, meant for use in cobalt beams, with a water-equivalent thickness of approximately 0.5 cm. The build-up cap surrounded the chamber, which was oriented perpendicularly to the beam axis. Such caps are generally not suitable for measurement of S_c at higher photon energies due to the presence of electron contamination.[12] A discussion on measurement techniques of S_c comes later in this report.

The purpose of this task group is to address the issues related to the determination, validation, and use of in-air output ratios for megavoltage photon beams from clinical linear accelerators. This task group report provides a comprehensive review of the current status including the clinical significance of the output ratio and the findings of the existing theoretical and experimental investigations. The report consist of self-contained sections: Section II focuses on the definition of essential dosimetry quantities; Sec. III and IV focus on the overall framework for the use of in-air output ratio in dose and monitor unit calculations and the various processes that contribute to S_c; Sec. V focuses on how to measure in-air output ratio; and Sec. VI and VII focus on practical methods for parametrization of S_c and quality assurance (QA) issues, respectively. Readers who are interested in the practical aspect of S_c measurement can jump to Sec. V since it contains the main recommendations of this report on how to determine S_c. Section VIII summarizes the main recommendations and clarifications of the report. Readers who are interested in how to parametrize S_c can jump to Sec. VI, although Sec. IV is essential for understanding various factors that affect S_c.

II. TERMINOLOGY

II.A. Photon beam and absorbed dose components

It is important to distinguish the terminology for photon beam components (e.g., primary or scattered photons), the quantities used to quantify the radiation (e.g., fluence), and the quantities used to describe the radiation impact (e.g., absorbed dose or ionization). It is often useful to separate the radiation incident on the patient into different components with distinguishable different dose deposition properties. The radiation is commonly separated based on the origin of radiation. **Direct radiation** is that photon radiation generated at the source that reaches the patient without any intermediate interactions. **Indirect radiation** is that photon radiation with a history of interaction/scattering with the flattening filter, collimators or other structures in the treatment unit head (see Fig. 1). Indirect radiation is commonly called **headscattered radiation** (or simply **headscatter**). Electrons and positrons released from interactions with either the treatment head or the air column constitute **charged particle contamination**, or in short, **electron contamination**. Together, the direct radiation, indirect radiation, and electron contamination comprise the **output radiation**, which from the patient point of view equals the **incident radiation**. The output (or incident) radiation is independent of the irradiated subject (i.e., patient; throughout this report, any reference to "patient" in a treatment situation will be understood to apply to a "phantom" in a measurement condition. Usually the terms simply imply a volume scattering medium.)

In the patient, charged particles released from the *first* interaction of the incident photons in the patient give rise to the **primary component of the absorbed dose**, also called the **primary dose** for short. For hypothetical points experiencing both lateral and longitudinal charged particle equilibrium (CPE), the primary dose is directly proportional to the

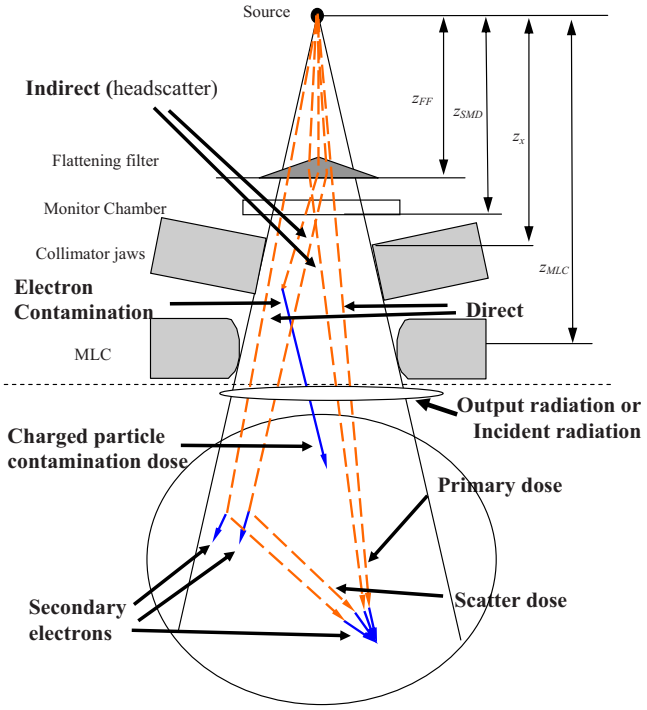

FIG. 1. Definition of general terms used in the task group report.

primary collision kerma to within a constant ($D_p = \beta K_p$) and it depends on the depth (or the attenuation of materials intersecting the beam along the ray line between the x-ray source and point of interest). Note that there can be a primary dose component from both the direct and indirect photons. The contribution to the absorbed dose from electrons released by photons scattered from elsewhere in the patient is called the **phantom scatter component of the absorbed dose**, in short the **scatter dose**. The scatter dose depends on the field size in the patient as defined by the collimation and the depth (these variables describe the scattering volume) and the incident fluence. The ratio of the scatter dose to the primary dose is called **scatter-to-primary ratio** (SPR) and is also expressed by the **scatter factor**,

$$\mathrm{SF}(s;d) = 1 + \mathrm{SPR}(s,d) = \frac{D(s;d)}{D_p(s;d)}, \tag{1}$$

which denotes the ratio of the total absorbed dose to the primary dose. The SPR depends on the field size in the patient and the depth and is almost independent of the source-to-skin distance (SSD) and other beam geometry parameters that affect the incident radiation. The absorbed dose from contaminant electrons is considered separately as **charged particle contamination dose** or **electron contamination dose** for short. This dose component cannot be further separated into primary and scatter parts since it stems from charged particles directly entering the patient. Table I summarizes the general terminology described in this section.

The definitions of the geometrical parameters characterizing a treatment head and a phantom are shown in Fig. 2. The collimator setting c is always specified at the isocenter at the source-to-axial distance (SAD) (usually 100 cm from the source). The field size, s, is always specified at depth d of measurement at the source-to-detector distance z (or SDD).

II.B. Output ratios

The **in-water output ratio**, S_{cp}, for a field of size s is defined as the ratio of the absorbed dose for the used collimator setting to the absorbed dose for the reference (or normalization) field size (s_{ref}), for the same MU, in a large water phantom at the same reference depth, d_{ref}, and the same reference source-to-detector distance, z_{ref}, on the central axis (commonly at the isocenter),

$$S_{cp}(c = s) \equiv \frac{D(c = s; z_{ref}; d_{ref})/\mathrm{MU}}{D(c_{ref} = s_{ref}; z_{ref}; d_{ref})/\mathrm{MU}}, \tag{2}$$

where D is the absorbed dose in the phantom, $c = s$ indicates that the field size of the phantom at depth d_{ref}, s, is that defined by the collimator setting, c, at the isocenter, usually 100 cm from the radiation source. The meaning of the water

TABLE I. Summary of terminology used to describe the output radiation. The first column shows the terms used for the sum of the components on respective row, while the bottom row shows the terms used to represent the sum of the components in the column above.

	Beam component					
	Direct radiation		Indirect radiation (headscatter)			
Interactions in patient	Open beam	Collimator leakage	Flattening filter scatter	Collimator scatter	Modulator scatter	Contaminant charged particles
Primary dose	Direct primary dose		Indirect primary dose			–
Scatter dose	Direct scatter dose		Indirect scatter dose			–
Charged particle contamination dose	–		–			Charged particle contamination dose
Total dose	Direct dose		Indirect dose (headscatter dose)			Charged particle dose

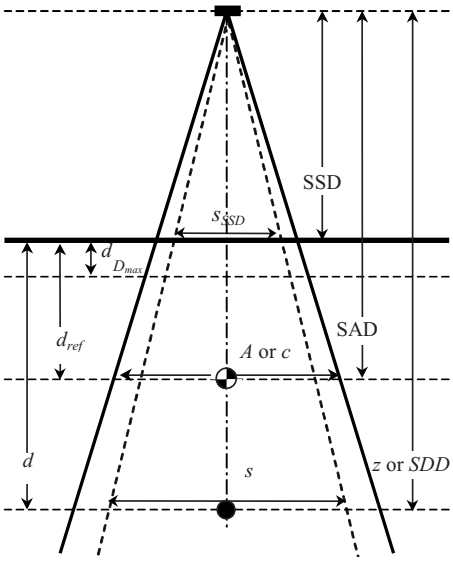

FIG. 2. Geometry for specifying output ratios. The reference depth is often at isocenter. The acronyms SSD, SAD and SDD are source-to-surface distance, source-to-axis distance, and source-to-detector distance. The dashed lines define the field size determined by an arbitrary block. The generic aperture variable, *A*, may, depending on context, represent the entire beam setup geometry rather than just collimator setting, *c*.

phantom being large is that it should enable full lateral and back scattering conditions for the field in question. The phantom should extend at least 9 cm in depth beyond the point of interest to ensure effectively full backscatter conditions for photon energy as low as cobalt-60.[13]

The **in-air output ratio**, S_c is now defined as the ratio of primary collision water kerma in free-space, K_p, per monitor unit between an arbitrary collimator setting, c, and the reference collimator setting, c_{ref}, at the same location on the central axis,

$$S_c(c) \equiv \frac{K_p(c;z_{ref})/\mathrm{MU}}{K_p(c_{ref};z_{ref})/\mathrm{MU}}, \tag{3}$$

where z_{ref} is the reference source-to-detector distance (usually $z_{ref}=100$ cm). Normally, the reference collimator setting is 10×10 cm^2, i.e., $c=10$ cm, for SAD = 100 cm. **Notice that the primary collision kerma excludes the scattered collision kerma induced by scatter from any surrounding phantom but includes all scattering that has occurred in the treatment head**. The main need for S_c is to quantify fluence variations with collimator settings for use in beam modeling and dose calculations. The idea behind the definition in Eq. (3) is to have a well defined quantity that is independent of experimental conditions yet closely related to energy fluence and primary dose. The collision kerma from photons is defined as the energy fluence for each energy times its mass energy absorption coefficient,

$$K_p \equiv \int_{\substack{\text{Primary}\\ \text{spectrum}}} \Psi_E \frac{\mu_{en}}{\rho} \mathrm{d}E. \tag{4}$$

The formal definition in Eq. (3) lends itself to the derivation of correction factors to compensate for any systematic deviations introduced by particular experimental methods used to estimate S_c, e.g., for differences in cap attenuation and filtration resulting from spectral differences between the arbitrary collimator setting and the reference setting (see Sec. V B).

For fields centered at points (x,y) off the axis of the collimator rotation ($x_{ref}=0$, $y_{ref}=0$), Eq. (3) becomes

$$S_c(c;x,y) \equiv \frac{K_p(c;x,y,z_{ref})/\mathrm{MU}}{K_p(c_{ref};x_{ref},y_{ref},z_{ref})/\mathrm{MU}}. \tag{5}$$

Experimentally, S_c can be estimated by the ionization ratio measured in a miniphantom that has sufficient thickness to eliminate electron contamination. The lateral dimensions of the miniphantom shall, besides eliminating contaminant electrons from the side, provide lateral electronic equilibrium at the detector. The material composition of the miniphantom must be carefully chosen as to minimize medium-induced deviations from water kerma ratios due to spectral differences between the beams c and c_{ref} or compensated by correction procedures (see Sec. V B). Measurement details are discussed later in Sec. V. When using a miniphantom and a detector, the ratio of primary collision kerma at the detector, K_p, can be expressed as[14]

$$\frac{K_p(c)}{K_p(c_{ref})} = \frac{\displaystyle\int_{\substack{\text{Primary spectrum}\\ \text{of beam } c}} \frac{\mu_{en}(E)}{\rho} \cdot \mathrm{e}^{-\mu(E)\cdot d} \cdot (\Psi_E(c;z_{ref})/\mathrm{MU}) \cdot \mathrm{SF}_K(\text{miniphantom}) \cdot \mathrm{d}E}{\displaystyle\int_{\substack{\text{Primary spectrum}\\ \text{of beam } c_{ref}}} \frac{\mu_{en}(E)}{\rho} \cdot \mathrm{e}^{-\mu(E)\cdot d} \cdot (\Psi_E(c_{ref};z_{ref})/\mathrm{MU}) \cdot \mathrm{SF}_K(\text{miniphantom}) \cdot \mathrm{d}E}, \tag{6}$$

where $\mu_{en}(E)/\rho$ is the mass energy absorption coefficient for the miniphantom medium at the photon energy E, $\mu(E)$ is the attenuation coefficient of the miniphantom medium, d is the depth in miniphantom (to the center of the detector sensitive volume), and $\Psi_E(c;z_{ref})$ and $\Psi_E(c_{ref};z_{ref})$ are the incident photon energy fluences (direct plus headscatter) at the miniphantom surface for the photon energy E for beam c and c_{ref}, respectively. $\mathrm{SF}_K(\text{miniphantom})=K/K_p$ is the ratio of

the total collision kerma to the primary collision kerma, or the kerma scatter factor, for the entire miniphantom. If the primary spectrum is independent of the collimation setting, then it follows that the signal ratio measures the energy fluence output ratio, $\int\Psi_E(c;z_{\mathrm{ref}})\mathrm{d}E/\int\Psi_E(c_{\mathrm{ref}};z_{\mathrm{ref}})\mathrm{d}E$. However, in situations where the beam quality is different from reference conditions (e.g., while using physical wedges), it must be noticed that the signal ratio is only an estimator of the energy fluence ratio, biased by the miniphantom and spectrum specific variations of collision kerma and attenuation.

A quantity more inclusive for different beam geometries is the **in-air output function** for the incident photon beam, O_{air}, defined as the ratio of primary collision water kerma in free-space per monitor unit for an arbitrary collimator setting (possibly with a beam modifier in place) and position, to the primary collision water kerma in free-space per monitor unit for the reference open beam under reference conditions (usually $c_{\mathrm{ref}}=10$ cm),

$$O_{\mathrm{air}}(c,B;x,y,z)\equiv\frac{K_{\mathrm{p}}(c,B;x,y,z)/\mathrm{MU}}{K_{\mathrm{p}}(c_{\mathrm{ref}};x_{\mathrm{ref}},y_{\mathrm{ref}},z_{\mathrm{ref}})\mathrm{MU}} \tag{7}$$

In the numerator, B represents all of the physical modifiers that may be in the beam, such as wedges, compensators, or trays. The use of O_{air} to map the lateral energy fluence variation for primary dose calculations will directly include the effects of off-axis variations in the energy absorption coefficient μ_{en}. Notice that in the absence of beam modifiers, O_{air} at the reference distance, z_{ref} is identical to the in-air output ratio, S_{c}. If it is desired to do in-air quantity based dosimetry with modifiers, K_{p} in the denominator of Eq. (7) refers to the reference open field without wedge at the reference conditions, thus O_{air} includes the transmission of the wedge filter while S_{c} does not. Similarly, the tray factor can be included in O_{air}. However, a common practice and the recommendation of AAPM TG71 makes the wedge factor and tray factor a ratio of doses in full phantom.[15] Either approach gives the same result but the corresponding MU formulation must be used.

The phantom scatter factor, S_{p}, is defined as the ratio of the scatter factors between the actual field size, s, in the phantom and that of the reference field size, s_{ref}, both at the reference depth, d_{ref},

$$S_{\mathrm{p}}(s)\equiv\frac{\mathrm{SF}(s;d_{\mathrm{ref}})}{\mathrm{SF}(s_{\mathrm{ref}};d_{\mathrm{ref}})}, \tag{8}$$

where SF is the ratio of the *total* dose in water (D) to the primary dose (D_{p}) for the same field setting and depth at the same location. Assuming that a particular collimator setting c equals the field size s at the isocenter, i.e., z is z_{ref}, the phantom scatter factor can, by using Eqs. (2) and (3), be determined using $K_{\mathrm{p}}(s)=D_{\mathrm{p}}(s)/\beta_p(s)$, by

$$\begin{aligned}\frac{S_{\mathrm{cp}}(s)}{S_{\mathrm{c}}(s)}&=\frac{D(s)}{D(s_{\mathrm{ref}})}\Bigg/\frac{K_{\mathrm{p}}(c=s)}{K_{\mathrm{p}}(c_{\mathrm{ref}}=s_{\mathrm{ref}})}\\&=\frac{D(s)/D_{\mathrm{p}}(s)}{D(s_{\mathrm{ref}})/D_{\mathrm{p}}(s_{\mathrm{ref}})}\cdot\frac{\beta_p(s)}{\beta_p(s_{\mathrm{ref}})}\\&=S_{\mathrm{p}}(s)\cdot\frac{\beta_p(s)}{\beta_p(s_{\mathrm{ref}})}\approx S_{\mathrm{p}}(s).\end{aligned} \tag{9}$$

Equation (9) shows that the requirement for the approximation $S_{\mathrm{p}}(s)\approx S_{\mathrm{cp}}(s)/S_{\mathrm{c}}(s)$ is that $\beta_p(s)/\beta_p(s_{\mathrm{ref}})$ is close to unity. This condition is fulfilled for all fields large enough to provide lateral electronic equilibrium. The intention of the phantom scatter factor is to describe the effects of photon scattering in the phantom only, and it follows that identical value of phantom scatter factors could be achieved for different collimator settings that result in equal amounts of phantom scatter at the point of interest. However, two fields that yield identical phantom scatter contributions from their respective direct component of the beams may give different scatter contributions in the phantom from the headscatter components since headscatter varies differently with collimation than the direct parts. This effect can be considered as small due to a rather large correlation between the shapes of the effective portals for the direct and indirect components of the beam, respectively.

III. THE ROLE OF S_c FOR MU CALCULATION

Dose calculation formalisms specify the parameters and their relationship to calculate monitor units from the prescribed dose. Given a particular formalism, its parameters may be estimated using very different methods, e.g., measurements, kernel-based convolution/superposition models, or Monte Carlo (MC) simulations, as long as the parameters are well defined in terms of the underlying physical interaction processes. Hence, a monitor unit formalism can be viewed as a framework, or "top level" model, within which different computation models can be implemented. We will here review two groups of formalisms, a factor-based formalism tailored for "hand" calculations and a model-based energy fluence formalism typical for modern treatment planning systems. Both calculation paths may use data, directly or indirectly, based on measurements of S_{c}.

III.A. Factor-based dose-to-dose ratio formalisms

Factor-based methods determine absorbed dose per monitor unit by using the product of standardized dose ratio measurements. Successive dose ratio factors are multiplied for a chain of geometries, and thus the dose ratio factors are varied one by one until the geometry of interest is linked back to the reference geometry,

$$\frac{D}{\mathrm{MU}}(\text{case A}) = \frac{(D/\mathrm{MU})_{\text{case A}}}{(D/\mathrm{MU})_{\text{case B}}} \cdot \frac{(D/\mathrm{MU})_{\text{case B}}}{\cdots} \cdot \frac{\cdots}{(D/\mathrm{MU})_{\text{ref}}} \cdot \frac{D}{\mathrm{MU}}(\text{ref}). \tag{10}$$

This equation is an identity equation. The strength of the formalism lies in that the calculations are simple and are based on the measured data. Obviously, one strives to use few and as general factors as possible, where some factors might be modeled instead of measured (e.g., the inverse square factor). The identity equation does not explain why $\mathrm{TPR}(s;d)$ is only a function of $(s;d)$ but not (z) and why $S_{cp}(c,s)=S_c(c)\cdot S_p(s)$. For that, one needs to introduce the concept of the separation of primary and scatter dose components. Analogous to the factorization in Eq. (10), one can construct collision kerma factors as means to formalize primary and scatter separation, i.e.,

$$\begin{aligned} D(c,s;z;d) &= \frac{D(c,s;z;d)}{K(c,s;z;d)} \cdot \frac{K(c,s;z;d)}{K_p(c,s;z;d)} \cdot K_p(c,s;z;d) \\ &= \beta(s;z;d) \cdot \mathrm{SF}_K(s;d) \cdot K_p(c;z;d), \end{aligned} \tag{11}$$

where $\beta=D(c,s;z;d)/K(c,s;z;d)$ is the dose-to-collision kerma ratio, $\mathrm{SF}_K=K(c,s;z;d)/K_p(c,s;z;d)=1+\mathrm{SPR}_K$ is the kerma scatter factor due to photon phantom scattering, and K_p is the primary collision kerma. $\mathrm{SF}_K=\mathrm{SF}$ under electron equilibrium. (One could use the dose-to-energy fluence ratio directly if a method to measure energy fluence could be developed.) The principle of the separation of primary and scatter components states that SF is only a function of phantom (depth and irradiated field size) and is independent of the source-to-detector distance, z, to the first order and collimator setting c; and β is a constant at sufficient depths, under transient charged particle equilibrium. K_p can be separated into components that are only correlated with the incident energy fluence $K_{inc}(c;z)$ and the transmission function $T(d)$ due to attenuation in the medium[16]

$$K_p(c;z;d) = K_{inc}(c;z) \cdot T(d). \tag{12}$$

The tissue-phantom ratio TPR and S_{cp} can be expressed as

$$\mathrm{TPR}(s;d) = \frac{D(c,s;z;d)}{D(c,s;z;d_{ref})} = \varepsilon(s;z;d) \cdot \frac{\mathrm{SF}(s;d)}{\mathrm{SF}(s;d_{ref})} \cdot \frac{T(d)}{T(d_{ref})} \tag{13}$$

and

$$\begin{aligned} S_{cp}(c,s) &= \frac{D(c,s;z;d_{ref})}{D(c_{ref},s_{ref};z;d_{ref})} \\ &= \frac{\varepsilon(s;d_{ref})}{\varepsilon(s_{ref};d_{ref})} \cdot \frac{\mathrm{SF}(s;d_{ref})}{\mathrm{SF}(s_{ref};d_{ref})} \cdot \frac{K_{inc}(c;z)\cdot T(d_{ref})}{K_{inc}(c_{ref};z)\cdot T(d_{ref})} \\ &\approx S_p(s)\cdot S_c(c), \end{aligned} \tag{14}$$

where $\varepsilon(s;d_{ref})=\beta(s;z;d)/\beta(s;z;d_{ref})$ is the electron disequilibrium factor ($\varepsilon=1$ for adequate depths and positions adequately far from the edges of the field). We assumed that d_{ref} is sufficiently large to establish electron equilibrium and shield from contamination electrons.

The accuracy of the factor-based dose calculation algorithms is determined by the accuracy of SF and S_c calculation under electron equilibrium conditions. S_c is very important in this formalism since it directly characterizes the variation in the incident collision kerma. The basic equation for dose calculation on the central axis at an arbitrary distance z can be derived using Eqs. (11)–(14) as

$$\begin{aligned} D(c,s;z;d) &= \mathrm{MU}\cdot\frac{D_{ref}(c_{ref},s_{ref};z_{ref};d_{ref})}{\mathrm{MU}}\cdot\frac{D(c,s;z;d)}{D_{ref}(c_{ref},s_{ref};z_{ref};d_{ref})} = \mathrm{MU}\cdot\frac{D_{ref}}{\mathrm{MU}}\cdot\frac{\varepsilon(s;z;d)\cdot K_{inc}(c;z)\cdot T(d)\cdot \mathrm{SF}(s;d)}{K_{inc}(c_{ref};z_{ref})\cdot T(d_{ref})\cdot \mathrm{SF}(s_{ref};d_{ref})} \\ &= \mathrm{MU}\cdot\frac{D_{ref}}{\mathrm{MU}}\cdot\frac{\varepsilon(s;z;d)\cdot T(d)\cdot \mathrm{SF}(s;d)}{T(d_{ref})\cdot \mathrm{SF}(s;d_{ref})}\cdot\frac{\mathrm{SF}(s;d_{ref})}{\mathrm{SF}(s_{ref};d_{ref})}\cdot\frac{K_{inc}(c;z)}{K_{inc}(c_{ref};z_{ref})} = \mathrm{MU}\cdot\frac{D_{ref}}{\mathrm{MU}}\cdot\mathrm{TPR}(s;d)\cdot S_p(s)\cdot O_{air}(c;z), \end{aligned} \tag{15}$$

where $D(c_{ref}=s_{ref};z_{ref};d_{ref})/\mathrm{MU}=D_{ref}/\mathrm{MU}$ is the dose per monitor unit under the reference conditions (usually collimator settings of 10×10 cm^2, 100 cm SAD, 10 cm depth), and using Eqs. (7) and (12) we can obtain

$$O_{air} = \frac{K_p(c;z)}{K_p(c_{ref};z_{ref})} = \frac{K_{inc}(c;z)}{K_{inc}(c_{ref};z_{ref})}. \tag{16}$$

O_{air} in Eq. (16) can be further separated into two factors as

$$O_{air}(c;z) = \frac{K_{inc}(c;z)}{K_{inc}(c_{ref};z_{ref})} = \frac{K_{inc}(c;z)}{K_{inc}(c;z_{ref})}\frac{K_{inc}(c;z_{ref})}{K_{inc}(c_{ref};z_{ref})} = \mathrm{DIST}(c;z)\cdot S_c(c), \tag{17}$$

$\mathrm{DIST}(c;z)=K_{inc}(c;z)/K_{inc}(c;z_{ref})$ is often approximated as $(z_{eff,ref}/z_{eff})^2$ where z_{eff} indicates the source-to-detector distance and the subscript "eff" means the source-to-point distance (SPD) fit to an inverse-square relationship.

The in-air output function, O_{air}, can be used for MU calculation for more general cases, e.g., for points off the axis and at an arbitrary distance from the source, where the dose can be expressed as

$$\begin{aligned}
D(c,s;x,y,z;d) &= \text{MU}\frac{D_{\text{ref}}}{\text{MU}}\frac{\varepsilon(s;x,y,z;\bar{d})K_{\text{inc}}(c;x,y,z)\text{SF}(s;x,y,z;\bar{d})T(x,y;d)}{K_{\text{inc}}(c_{\text{ref}};x_{\text{ref}},y_{\text{ref}},z_{\text{ref}})\text{SF}(s_{\text{ref}};x_{\text{ref}},y_{\text{ref}},z_{\text{ref}};d_{\text{ref}})T(x_{\text{ref}},y_{\text{ref}};d_{\text{ref}})} \\
&= \text{MU}\frac{D_{\text{ref}}}{\text{MU}}\frac{\text{SF}(s;x,y,z;d_{\text{ref}})}{\text{SF}(s_{\text{ref}};x_{\text{ref}},y_{\text{ref}},z_{\text{ref}};d_{\text{ref}})}\frac{\varepsilon(s;x,y,z;d)\text{SF}(s;x,y,z;\bar{d})T(x,y;d)}{\text{SF}(s;x,y,z;d_{\text{ref}})T(x,y;d_{\text{ref}})} \\
&\quad\times\frac{K_{\text{inc}}(c;x,y,z)\cdot T(x,y;d_{\text{ref}})}{K_{\text{inc}}(c_{\text{ref}};x_{\text{ref}},y_{\text{ref}},z_{\text{ref}})\cdot T(x_{\text{ref}},y_{\text{ref}};d_{\text{ref}})} \\
&= \text{MU}\frac{D_{\text{ref}}}{\text{MU}}\frac{\text{SF}(s;x,y,z;d_{\text{ref}})}{\text{SF}(s_{\text{ref}};x_{\text{ref}},y_{\text{ref}},z_{\text{ref}};d_{\text{ref}})}\frac{\varepsilon(s;x,y,z;\bar{d})\text{SF}(s;x,y,z;\bar{d})T(x,y;d)}{\text{SF}(s;x,y,z;d_{\text{ref}})T(x,y;d_{\text{ref}})}\frac{K_{\text{p}}(c;x,y,z)}{K_{\text{p}}(c_{\text{ref}};x_{\text{ref}},y_{\text{ref}},z_{\text{ref}})} \\
&= \text{MU}\frac{D_{\text{ref}}}{\text{MU}}S_{\text{p}}(s;x,y)\cdot\text{TPR}(s;x,y;\bar{d},d)\cdot O_{\text{air}}(c;x,y,z) \\
&\approx \text{MU}\frac{D_{\text{ref}}}{\text{MU}}S_{\text{p}}(s')\cdot\text{TPR}(s';\bar{d},d)\cdot O_{\text{air}}(c;x,y,z). \qquad (18)
\end{aligned}$$

In this equation, c_{ref} is the reference field (10×10 cm^2) that is centered on the collimator axis. $\bar{d}$ and d are the average depth and the depth along the ray line (x,y) from the x-ray source, respectively. The equivalent square, s', for the off-axis point (x,y) is chosen so that $\text{SF}(s';x_{\text{ref}},y_{\text{ref}};d)=\text{SF}(s;x,y;d)$, where s is the square field centered on the central axis. The equivalent square for an arbitrary point in the field, s', can be determined using the measured SF for circular fields on the central-axis and the scatter integration.[17] The definition of the TPR has been expanded for application to rays off the collimator axis, but keeping the numerator and denominator on the same ray. Off-axis beam-softening renders $\text{TPR}(s;x,y;\bar{d},d)$ different from $\text{TPR}(s';x_{\text{ref}},y_{\text{ref}};\bar{d})$.[18] Further details are beyond the scope of this report.

In Eq. (18), O_{air} can be separated as

$$\begin{aligned}
O_{\text{air}}(c;x,y,z) &= \frac{K_{\text{inc}}(c;x,y,z)\cdot T(x,y;d_{\text{ref}})}{K_{\text{inc}}(c_{\text{ref}};x_{\text{ref}},y_{\text{ref}},z_{\text{ref}})\cdot T(x_{\text{ref}},y_{\text{ref}};d_{\text{ref}})} = \frac{K_{\text{inc}}(c;x,y,z)}{K_{\text{inc}}(c;x,y,z_{\text{ref}})}\cdot\frac{K_{\text{inc}}(c;x,y,z_{\text{ref}})\cdot T(x,y;d_{\text{ref}})}{K_{\text{inc}}(c_{\text{ref}};x_{\text{ref}},y_{\text{ref}},z_{\text{ref}})\cdot T(x_{\text{ref}},y_{\text{ref}};d_{\text{ref}})} \\
&= \text{DIST}(c;x,y,z)\cdot S_{\text{c}}(c;x,y). \qquad (19)
\end{aligned}$$

For off-axis points, S_{c} was defined by Eq. (5) in Sec. II B. Notice that the definition of S_{c} includes the variation of the incident radiation with the point off the axis. For points within 4 cm of the collimator axis, the value for S_{c} at off-axis point is very close to that on the central axis for points well within beam collimation.[19]

For a wedged beam, S_{c} defined in Eq. (19) is now denoted as $S_{c,w}$, i.e.,

$$\begin{aligned}
O_{\text{air},w}(c;x,y,z) &= \frac{[K_{\text{p}}(c;x,y,z)]_{\text{wedge}}}{[K_{\text{p}}(c_{\text{ref}};x_{\text{ref}},y_{\text{ref}},z_{\text{ref}})]_{\text{open}}} = \frac{[K_{\text{p}}(c;x,y,z)]_{\text{wedge}}}{[K_{\text{p}}(c;x,y,z_{\text{ref}})]_{\text{wedge}}}\cdot\frac{[K_{\text{p}}(c;x,y,z_{\text{ref}})]_{\text{wedge}}}{[K_{\text{p}}(c_{\text{ref}};x_{\text{ref}},y_{\text{ref}},z_{\text{ref}})]_{\text{wedge}}}\cdot\frac{[K_{\text{p}}(c_{\text{ref}};x_{\text{ref}},y_{\text{ref}},z_{\text{ref}})]_{\text{wedge}}}{[K_{\text{p}}(c_{\text{ref}};x_{\text{ref}},y_{\text{ref}},z_{\text{ref}})]_{\text{open}}} \\
&= \text{DIST}_w(c;x,y,z)\cdot S_{c,w}(c;x,y)\cdot\text{WF}_{\text{air}}(c_{\text{ref}}). \qquad (20)
\end{aligned}$$

This would give a formula for calculating MU for a wedged beam as

$$\text{MU} = \frac{D(c,s;x,y,z;d)}{\frac{D_{\text{ref}}}{\text{MU}}\cdot S_{p,w}(s')\cdot\text{TPR}_w(s';\bar{d},d)\cdot S_{c,w}(c;x,y)\cdot\text{WF}_{\text{air}}(c_{\text{ref}})\cdot\text{DIST}_w(c;x,y,z)}, \qquad (21)$$

where $\text{WF}_{\text{air}}(c_{\text{ref}})$ is the in-air wedge factor for the reference condition, DIST_w is the inverse-square distance factor, and $S_{p,w}(s')$ is the phantom scatter factor for the wedged beam. $S_{c,w}$ as defined in this report for a wedged beam is often not used in conventional MU calculation algorithms. The formalism from more conventional equation has the form,

$$\text{MU} = \frac{D(c,s;x,z;d)}{\frac{D_{\text{ref}}}{\text{MU}}\cdot S_{\text{p}}(s')\cdot\text{TPR}(s';\bar{d})\cdot S_{\text{c}}(c;x_{\text{ref}},y_{\text{ref}})\cdot\text{WF}(c;x,d)\cdot\text{POAR}(x,y;d_{\text{ref}})\cdot\text{DIST}(z)}, \qquad (22)$$

where S_c for open beam alone is used, and the headscatters from wedge fields are lumped into a field size dependent wedge factor, $\mathrm{WF}(c;x;d)$, where the wedge gradient is in the x direction. Users are cautioned to avoid double counting the in-air output ratio if a field size dependent wedge factor is used. The POAR is the primary off-axis ratio measured at depth d_{ref} in a miniphantom for the largest collimator setting. Detailed derivation can be found in Appendix B.

III.B. Model-based dose-to-energy fluence formalisms

The absorbed dose resulting from an irradiation is directly proportional to the energy fluence incident onto the patient. This makes normalization of the calculated dose per energy fluence appealing. Energy fluence is more practical than particle fluence since the kerma per energy fluence is only weakly dependent on photon energy. Thus, this application of the formalism is robust for small shifts in beam quality. Both kernel-based convolution/superposition models and Monte Carlo-based calculations can be implemented using such a formalism since the absorbed dose can be calculated per monitor unit following a "global" energy fluence to monitor units calibration. Details of such a formalism have been outlined by Ahnesjö and co-workers[19–21] and Mackie *et al.*[22] The core of the dose calculation engine is supposed to deliver the quantity, dose to energy fluence ratio, ω,

$$\omega(x,y,z) = \frac{D(x,y,z;\Psi(A;x,y,z_{\mathrm{ref}}))}{\Psi_0}, \tag{23}$$

where $D(x,y,z;\Psi(A;x,y,z_{\mathrm{ref}}))$ is the absorbed dose at point (x,y,z), given that the lateral energy fluence distribution for the applicator setting A, $\Psi(A;x,y,z_{\mathrm{ref}})$ is defined free in-air at a reference distance z_{ref} from the source, and Ψ_0 is the energy fluence of direct photons free in-air at the isocenter. Following Ahnesjö *et al.*,[23] the MU registered for a given beam can be separated into two parts, $\mathrm{MU}=\mathrm{MU}_0+\mathrm{MU}_b$ where MU_0 is the signal proportional to the forward fluence through the monitor chamber and $\mathrm{MU}_b=b(A)\cdot\mathrm{MU}_0$ is proportional to the fluence of particles backscattered into the monitor from the upper sides of the adjustable collimators. The total energy fluence delivered free in-air per monitor unit can thus be written as

$$\begin{aligned}\frac{\Psi(A;x,y,z_{\mathrm{ref}})}{\mathrm{MU}} &= \frac{\Psi(A;x,y,z_{\mathrm{ref}})}{\Psi_0}\cdot\frac{\Psi_0}{\mathrm{MU}_0+\mathrm{MU}_b} \\ &= \frac{\Psi(A;x,y,z_{\mathrm{ref}})}{\Psi_0}\cdot\frac{\Psi_0}{\mathrm{MU}_0}(1+b(A))^{-1}. \end{aligned}\tag{24}$$

The ratio Ψ_0/MU_0 provides the key link between the absorbed dose per energy fluence as calculated by the dose calculation engine and the absorbed dose per monitor unit as needed for monitor unit settings. This ratio is directly derived from the monitor backscatter corrected ratio of dose calculated and measured for the reference geometry according to

$$\frac{\Psi_0}{\mathrm{MU}_0} = \frac{[D(A;x_{\mathrm{ref}},y_{\mathrm{ref}},z_{\mathrm{ref}})/\mathrm{MU}]_{\mathrm{Measured}}}{[D(A;x_{\mathrm{ref}},y_{\mathrm{ref}},z_{\mathrm{ref}})/\Psi_0]_{\mathrm{Calculated}}}(1+b(A_{\mathrm{ref}})), \tag{25}$$

where $\mathrm{MU}=\mathrm{MU}_0(1+b(A))$ have been used.

Modeling of the energy fluence is commonly done separately for the direct and indirect photons, respectively. The direct photons are simply given by blocking collimated parts in a relative distribution of the direct photons for an uncollimated beam to yield the relative distribution $f(A;x,y,z_{\mathrm{ref}})$. Adding indirect photons, Ψ_{ind}, from irradiated parts of the treatment head then yields the total photon energy fluence of the beam,

$$\Psi(A;x,y,z_{\mathrm{ref}}) = \Psi_0\cdot\left(f(A;x,y,z_{\mathrm{ref}}) + \frac{\Psi_{\mathrm{ind}}(A;x,y,z_{\mathrm{ref}})}{\Psi_0}\right), \tag{26}$$

where f is the relative energy fluence of direct particles.

Equations (23)–(26) specify a framework for model-based dose calculations. To calculate the absorbed dose, fluence must be modeled such that the energy fluence distributions of both direct and indirect particles are provided relative to the reference fluence of direct particles Ψ_0 as well as the collimator backscatter to the monitors through $b(A)$.

Writing the in-air output ratio on the central axis as an energy fluence ratio (assuming the mass energy absorption coefficient does not change with aperture setting A) shows the role for the measured data,

$$\begin{aligned} S_c &\approx \frac{\Psi(A;z_{\mathrm{ref}})/\mathrm{MU}}{\Psi(A_{\mathrm{ref}};z_{\mathrm{ref}})/\mathrm{MU}} \\ &= \frac{\Psi_0+\Psi_{\mathrm{ind}}(A)}{\Psi_0+\Psi_{\mathrm{ind}}(A_{\mathrm{ref}})}\cdot\frac{(1+b(A_{\mathrm{ref}}))}{(1+b(A))} = S_h\cdot S_b. \end{aligned}\tag{27}$$

where S_h is the headscatter factor and S_b is the monitor backscatter factor. We have used Eqs. (3), (24), and (26) in the derivation. The most direct way of determining parameters for headscatter models is through matching the model results to measured S_c data since it directly depends on the variation in headscatter and monitor backscatter. In Sec. IV, we will review the physical processes leading to the variation in $\Psi_{\mathrm{ind}}/\Psi_0$, with varying field settings, and the main approaches used for its modeling.

IV. PHOTON BEAM CHARACTERISTICS

Different approaches have been investigated to derive the beam characterization data for dose calculations. The Monte Carlo method has proven useful in analyzing the various components of the output ratio, an approach pioneered by Nilsson and Brahme[24] and later systematically implemented in the BEAM package,[25] which has been used extensively in photon beam modeling. A practical approach that avoids handling of extensive phase space data sets is to use comprehensive "multisource" models, and then to derive the model parameters from measured S_c. This approach is self-consistent and has been implemented for Varian, Siemens, Elekta, and other clinical accelerators.[26–30] At best, such models are developed based on the analysis of Monte Carlo simulated beam data, and the model parameters can have clear physical interpretation. Multiple source models assume that particles in a radiotherapy beam are from different subsources representing major contributing components of a clinical accelera-

tor. For example, a point (or extended) photon source represents direct photons from the target, an extended extrafocal photon source represents scattered photons from the primary collimator, the flattening filter and the ion chamber, and an extended electron source represents contaminant electrons.[26,28,31–33] A source model might have slightly different subsource geometries for different linac models but the model parametrization is basically generic for commonly used clinical accelerators. A detailed model would provide the time independent energy fluence $\Psi_{E,\Omega}$, differential in energy and direction at all points (x,y,z_{ref}) in a beam at the reference plane, z_{ref}, all normalized per monitor unit signal. In practice, the fluence monitoring is nontrivial since scattered photons from the treatment head add an "unmonitored" contribution to the fluence, and backscatter into the monitor yields a "false" contribution to the total signal

$$\frac{\Psi}{\mathrm{MU}} = \frac{\Psi_0 + \Psi_{\mathrm{ind}}}{\mathrm{MU}_0 + \mathrm{MU}_b}. \tag{28}$$

It is therefore common to describe the direct beam Ψ_0 and the indirect components Ψ_{ind} of the beam separately as we will do in the following sections. We will briefly review photon beam characteristics based on experimental investigations, Monte Carlo simulations, and analytical studies and modeling. Related reviews exist on multisource modeling,[34] on dose calculations,[35] and on Monte Carlo linac simulation methods.[36,37]

IV.A. Photon spectra and direct beam fluence distribution

Given an energy fluence spectrum of direct photons, many dosimetric quantities such as attenuation, kerma, etc., are trivial to calculate directly using generally available tabulations of interaction data. Hence there has been a great interest to determine the beam spectra. Monte Carlo simulations and several reconstructive techniques from attenuation or depth dose measurements have been explored.

In a much cited study, Mohan *et al.*[38] used Monte Carlo to determine spectra for 4–24 MV photon beams from Varian accelerators. Recent comparisons with more sophisticated MC simulations[39,40] showed that the spectra of Mohan *et al.* still represent a fair approximation. For accurate results, Monte Carlo simulations require tuning of the electron beam properties based on the measured beam data.[39,41] Sheikh-Bagheri and Rogers[39] performed a thorough MC study of nine photon beams in the energy range of 4–25 MV from Varian, Siemens, and Elekta linacs. An important result was to point out that in-air dose profiles measured with an ion chamber and a proper build-up cap is the most effective experimental data to match simulation results while varying the energy and spatial characteristics of the primary electron beam.

Reconstructive techniques based on depth dose or attenuation is an appealing alternative to full Monte Carlo simulations since the reconstruction process in itself implies consistency with end result verification data such as depth doses. The main difficulty in reconstructive techniques is the poor numerical conditioning of photon spectrum unfolding, which makes the use of spectral shape constraints necessary. Also, the absorbed dose from charged particle contamination in the build-up region must be considered while including the data from the build-up region. Ahnesjö and Andreo[42] combined a parametrized model for charged particle contamination with a semianalytical spectrum model whose parameters were varied to minimize the difference between the measured depth doses and the depth doses reconstructed from the sum of the absorbed dose for a pure photon beam and the charged particle dose. In a similar dose reconstructive approach, Sauer and Neumann[43] used general shape properties of realistic spectra imposing positivity and monotony requirements. Methods based on attenuation data have also been employed.[44–50] Most of these studies also used constraints on the spectral shape to handle numerical conditioning problems.

The spectra at off-axis positions are "softer," i.e., have a lower mean or effective energy, than those at the central axis. In a broad experimental survey involving 15 different linac beams, Tailor *et al.*[18] showed that the relative change, with off-axis angle, of the narrow beam half value thickness had a similar shape for all investigated machines, also confirmed by earlier data from Yu *et al.*[51] and Bjärngard and Shackford.[16] Although these general parametrizations exist, off-axis beam quality variations depend on the material of the flattening filter[52] and should therefore be at least checked as part of the machine commissioning procedure. The check can be easily performed by comparing calculation and measurement of D/MU at an off-axis point at depths larger or equal to 20 cm in a large enough field.

Off-axis variations in the energy fluence depend on the design of the flattening filter and the energy of the electron beam hitting the target. The in-air output function [Eq. (7)] is an obvious option based on direct measurements using build-up cap that directly includes the kerma bias (i.e., multiplication of μ_{en}/ρ to the energy fluence) needed for correct primary dose calculation. Treuer *et al.*[53] and Ahnesjö and Trepp[54] worked out procedures to allow for full lateral mappings of general, nonrotational symmetrical beams based on deconvolution of a dose distribution measured in a lateral plane with respect to the beam axis.

Physical wedges and compensating filters, if present, change the beam spectrum. van der Zee and Welleweerd[55] simulated the Elekta internal wedge. They found that the presence of the wedge altered the primary and scattered photon components from the linac significantly: Beam hardening shifted the mean photon energy by 0.3 and 0.7 MeV for the two components, respectively, for a 10 MV photon beam. Soft wedges such as dynamic or virtual wedges have, on the other hand, proven not to introduce any significant spectral changes as contrast to physical wedges.[56–58,27] The consequences from spectral changes in terms of change in primary and scatter dose deposition pattern with depth have been further analyzed and modeled.[20]

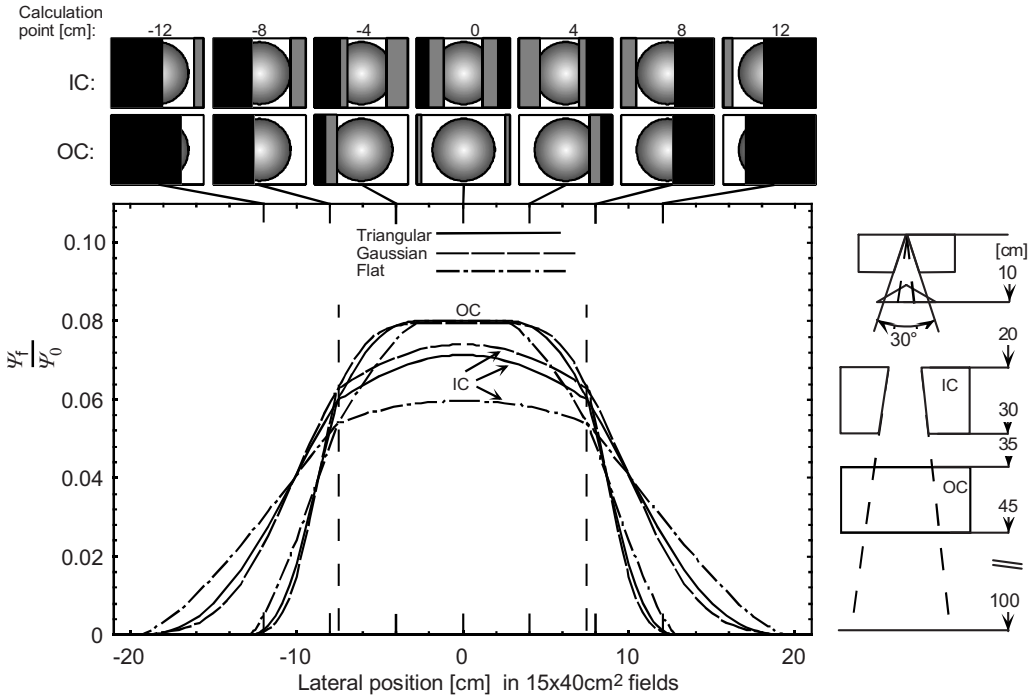

FIG. 3. Flattening filter scatter profiles (normalized to the isocenter primary energy fluence Ψ_0) at the isocenter plane for two 15×40 cm^2 fields defined by the inner (IC) and outer (OC) collimators. The profiles are along the 15 cm axis; the machine geometry is shown to the right. The calculation's point eye view of the filter at various positions is shown on top of the chart. Three different distributions of scatter release from the filter are compared; a triangular, a Gaussian and a flat (constant) distribution, all normalized to yield 8% scatter at isocenter when the entire filter is viewed [from Ahnesjö (Ref. 19)].

IV.B. Photon scatter from the flattening filter and primary collimator

The scatter from the flattening filter acts as an extended source, a concept in beam modeling that has been explored and refined over the years. Measurements,[4,6,8–10,59–64] Monte Carlo simulations,[38,65,66] and analytic approximations[19] have all established the role of the flattening filter and the primary collimator as a distributed source which may contribute up to 12% of the output photons. Distributed-source models have been used to calculate output ratios on the central axis of arbitrarily shaped fields.[19,23,63,65,67,68] Most variation in the in-air output ratio with field size and position can be explained through modeling the number of scattered photons by an extended source integration over the part of the linac head visible from the calculation's point of view[4,8,10,19,23,63,65,69] (see Fig. 3). These characteristics of photon beams stem from a partial eclipsing of the extrafocal source by the field defining collimators. Different intensity distributions of the extended source have been used in the simulation, such as triangular, constant, or Gaussian functions, yielding similar results indicating that the actual area of the filter being exposed to the primary beam is more important than the particular intensity distribution used to model it. Beam models that employ extrafocal source distributions and the geometry of the treatment head can predict the change of headscatter and beam penumbra with field size. Since the flattening filter is located downstream from the target and introduces an extended photon source, which will reach outside of the beam collimation where it will dominate since the collimator leakage contribution is even less. Experimental data confirm these findings.[70] Several studies also show up to 2% variation in S_c values at off-axis locations inside beam collimation.[62,70–72]

It must be emphasized that because the dose contribution from headscattered photons usually dominates the dose distribution outside the beam, accounting for indirect radiation is very important for the prediction of absorbed dose in such locations. An off-axis headscatter model is thus very important to accurately predict the absorbed dose at off-axis points.[70] Figure 4 shows the measured lateral distribution of

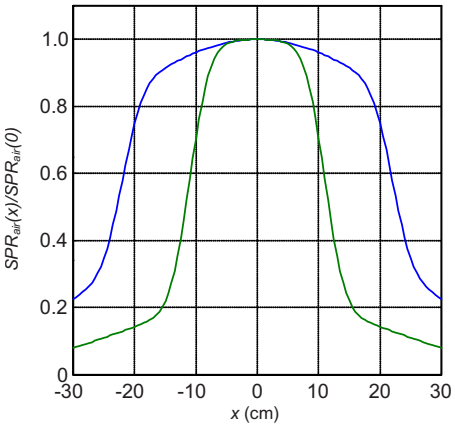

FIG. 4. Measured $\mathrm{SPR}_{\mathrm{air}}(c;x)/\mathrm{SPR}_{\mathrm{air}}(c;0)$ for two collimator settings: $c=20$ and 40 cm. All curves are normalized to 1 for $x=0$. $\mathrm{SPR}_{\mathrm{air}}(c;x)$ is the scatter-to-primary kerma ratio between headscatter and direct photons for collimator setting c at off-axis position, x (see text for details). [Adapted from Zhu *et al.* (Ref. 70)].

normalized scatter-to-primary ratio, $SPR_{air}(c;x)/SPR_{air}(c;0)$, for headscatter and direct components of a 6 MV photon beam from a Varian accelerator for two different collimator settings $c=20$ and 40 cm. The curves are obtained by fitting two Gaussian-source models for $SPR_{air}(c;x)$ to $S_c(c;x)/POAR(x)$, where $S_c(c;x)$ is the in air output ratio as defined by Eq. (5) and $POAR(x)$ is the primary off-axis ratio.[70]

Since the flattening filter scatter may constitute up to 12% of the output photon radiation, its location downstream of target will influence the variation in incident radiation as a function of patient distance to the x-ray source, a phenomenon that can be modeled through the use of a virtual source position. It has been shown that the virtual source position was about 1 cm downstream of the target for an open field and about 2–3 cm for a wedged field from Elekta, which has an internal physical wedge.[7] A more detailed study to examine the correlation between S_c and SDD showed that the change in S_c for open beam at different SDD is indeed very small (<1%) for SDD up to 300 cm.[73] A similar study for wedged beams estimated that the change in S_c at different SDD is about 2% for wedged beams.[74]

IV.C. Wedge and compensator scatter

The presence of a wedge or a compensating filter increases the fraction of headscattered photons, and hence the variation in S_c with changes in collimation.[8] In principle, one should account for the headscatter source from the wedge and the flattening filter separately.[20,75] Due to the difference in geometry, one can anticipate different field size dependence of S_c between an internal wedge and an external wedge.[75] The former is mounted inside the accelerator head and always completely irradiated but not always completely seen through the collimator opening, while the latter is irradiated only by the collimated beam, always completely seen from the point of interest and also closer to the patient compared to the former.

Analytical calculation models based on first scatter integration over the scattering device[20,76] and an "extended phantom concept" using precalculated modulator kernels superimposed over the modulator within the calculation point of view[77] have all shown good agreement. Monte Carlo simulations confirm and bring further details to these results. Schach von Wittenau *et al.*[78] investigated to which degree Monte Carlo simulations can be approximated without changing the result.

IV.D. Collimator scatter and leakage

Detailed jaw and MLC geometries have been studied for different accelerators using Monte Carlo simulations[79,80,26,81] and analytical models.[82] Collimators play an important role in defining scatter contributions from the treatment head through partial obscuring of structures such as target, primary collimator, and flattening filter. The scatter contributions from the movable collimators themselves are less than 1% of the total dose[123] (about one-tenth that of the total headscatter), but rounded MLC edges might add more scatter. The photon leakage through the bulk of the jaws is generally less than 0.5% although the interleaf leakage in between MLC leaves can be 1%–2%.[83] van de Walle *et al.*[84] simulated the 80-leaf Elekta SLiplus MLC. They showed that the interleaf leakage hardens the transmitted radiation by about 0.15 MeV for a 6 MV photon beam and noted significant differences for photon spectra under the leaf body compared to under the leaf gap. Deng *et al.*[85] studied the MLC tongue-and-groove effect on IMRT dose distributions. Based on the actual leaf sequence and MLC leaf geometry, they derived a fluence map using a ray-tracing approach for an IMRT plan. Their results suggest that the effect of the tongue-and-groove geometry is probably insignificant in IMRT with multiple gantry angles, especially when organ/patient movement is considered.

For blocks, Thatcher and Bjärngard[86] pointed out that they should in most cases have a negligible effect on S_c (at most a 1% change for most clinic cases including extreme blocks) because the collimator jaws are located closer to the location of the flattening filter than the blocks, thus it is the collimator jaws rather than the blocks that influence the amount of headscatter from the flattening filter. Jursinic, however, noticed a headscatter effect of up to 2% due to photon scattering from the tray and the block.[87] van Dam *et al.*[88] examined the effect of the block on a large number of accelerators and quantified its variation to be < 1%. Higgins *et al.*[89] performed an exhaustive study and quantified the effect of the block on S_c to be 1%.

IV.E. Monitor backscattering

Photon backscatter from the collimator jaws into the monitor chamber may, for collimators located close to the monitor, have a significant effect on output for some accelerators. As pointed out through Eq. (24), the total output from a machine may be less than monitored due to a perturbation signal MU_b caused by backscattered particles. The monitor backscatter has been studied by a variety of experimental methods. Techniques for measuring $b=MU_b/MU_0$ include activation of metal foils,[60] using a pinhole telescope aimed at the target,[90–93] comparing output differences with and without an acrylic filter between the chamber and the jaws,[61] counting beam pulses,[10,93,94] measuring beam current,[95] and measuring beam charge.[92] Kubo[90] used a telescopic technique to exclude the scattered components from the readout of an external detector and measured the variation in monitor units delivered per unit external signal. For a Clinac 1800, he found small variations (1%–2%) between small and very large collimator settings. For a Therac 20 machine, however, the backscatter variation was as high as 7.5% (cf. Fig. 5). Hounsell[96] also used a telescopic technique and found small variations of the order of less than 1% for an Elekta-Philips SL15 with a protection sheet (3 mm Al) in place between the collimators and the monitor chamber. The variation was considerably higher when the protection sheet was removed, approximately 5% between the 4×4 and 40×40 cm^2 field. Several investigators[10,93,97] used the number of linac pulses as an independent measure of the primary

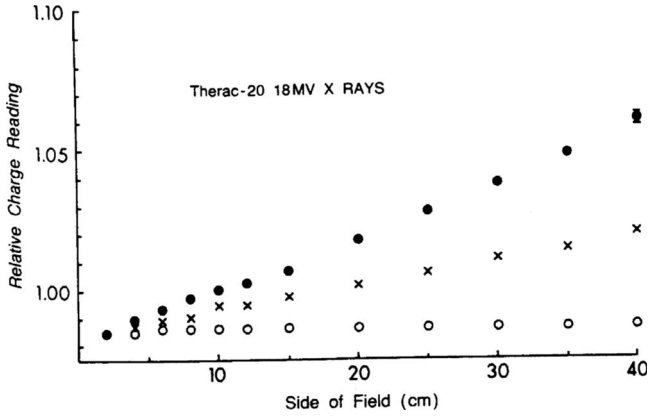

FIG. 5. Results of monitor backscattering obtained by a telescopic method with an 18 MV x-ray from a Therac-20 accelerator. Different symbols represent different collimator settings: ●—square fields; ×—fixed inner jaws; ○—fixed outer jaws. [Adapted from Kubo (Ref. 90)].

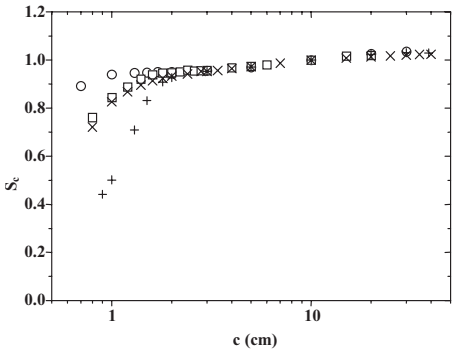

FIG. 6. Measured S_c for open field of four accelerators are shown. ○—Varian Clinac 1800, 10 MV, □—Philips SL25, 6 MV, ×—Philips SL75-5, 6 MV, +—Varian Clinac 6/100, 6 MV. [Adapted from Zhu *et al.* (Ref. 100)].

fluence and found that the monitor backscatter signal varied from 2% to 5% for the largest to the smallest fields with a kapton window monitor chamber. When a protection sheet of aluminium was set in place to stop low energy charged particles, the variation reduced to 0.5%–1.0%. Yu *et al.*[93] applied this technique to a Varian Clinac 600C and 2100C and found a variation of approximately 2% for the inner jaws and 1% for the outer jaws at energies above 15 MV, and about half of those values for 6 MV. Lam *et al.*[92] measured the target charge needed to deliver a given number of monitor units as a function of collimator setting, as it was considered more reliable than the number of linac pulses. On a Varian Clinac 2100C, they found a 2.4% variation for the upper jaws and 1.0% variation for the lower pair of jaws. More recent measurements have shown that the monitor backscatter factors for a flattening filter free accelerator have the same magnitude as that for the same accelerator with the flattening filter.[98] In general, all methods to explicitly measure S_b are rather cumbersome, and to various degrees invasive to the accelerator structure or controls and cannot be recommended for routine use.

Using Monte Carlo, Verhaegen *et al.*[99] and Ding[66] modeled the photon beams in a Varian Clinac 2100C linac. By tagging particles and selectively transporting photons and electrons, they found that low energy electrons cause most of the backscatter effect.

An analytical model for the backscatter signal fraction $b = \mathrm{MU}_b/\mathrm{MU}_0$ has been proposed by Ahnesjö *et al.*[23] assuming that it can be determined by a proportionality factor k_b times a geometry factor for backscatter radiation,

$$b = k_b \frac{z_{\mathrm{SMD}}^2}{z_{\mathrm{SCD}}^2} \int_{\hat{A}} \int \frac{\cos^3 \theta_A}{\pi \cdot z_{\mathrm{MCD}}^2} \mathrm{d}\hat{A}, \tag{29}$$

where z_{SMD} is the source to monitor distance, z_{SCD} is the distance from the source to the backscattering collimator surface, z_{MCD} is the monitor to backscattering surface distance, θ_A is the angle between the normal of the backscattering element $\mathrm{d}\hat{A}$ and its view vector of the monitor, and $\hat{A}$ is the irradiated backscattering area. (In the original paper source-to-isocenter distance was erroneously used instead of z_{SMD} and the reflected radiation stated to be isotropic rather than diffuse.) A comparison of data from the work of Lam *et al.*[92] versus Eq. (29) yields k_b values of the order of 0.3–0.4 for Kapton windowed chambers and approximately zero for chambers with metal sheet windows.

Since $b = \mathrm{MU}_b/\mathrm{MU}_0$ decreases with increasing field size (less backscattering area), $S_b = (1 + b(A_{\mathrm{ref}}))/(1 + b(A))$ will increase with collimator settings. Hence, the net effect of monitor backscatter is to increase the output per monitor unit with increasing field size, as the scatter fluence from extended sources does.

IV.F. Direct source obscuring effect

For very small collimator settings (usually less than 2×2 cm^2), the target, i.e., the effective x-ray source, is partially obscured by the collimator jaws resulting in a substantial reduction in the output.[100] Due to the finite source size, S_c is expected to reduce to zero when the collimator jaws are completely closed. The source-obscuring effect dominates the output ratio for very small fields at low energies.[101] For higher energies, the loss of lateral electron equilibrium becomes more important. For all energies, it is important that during measurement the open part of the beam covers both the detector and the entire build-up phantom.

Not only the size but also the shape of the source, as affected by the beam transport system, are of importance for small fields. Figure 6 shows the measured S_c values for several different accelerators.[100] The greatest effect is shown for the Clinac-6/100, which has no bending magnet. The next largest effect shown is from the SL75-5 with a 90° permanent bending magnet. The SL25 has a 90° bending magnet as well, but it is preceded by a "slalom" magnet arrangement. The Clinac-1800 with a 270° bending magnet and an electron slit shows the smallest effect and has the smallest x-ray source size among the accelerators examined. Zhu *et al.*[11] demonstrated that one can reconstruct the shape of the x-ray source with S_c, measured for a series of slit collimator settings at different collimator angles. Jaffray *et al.*[9] presented

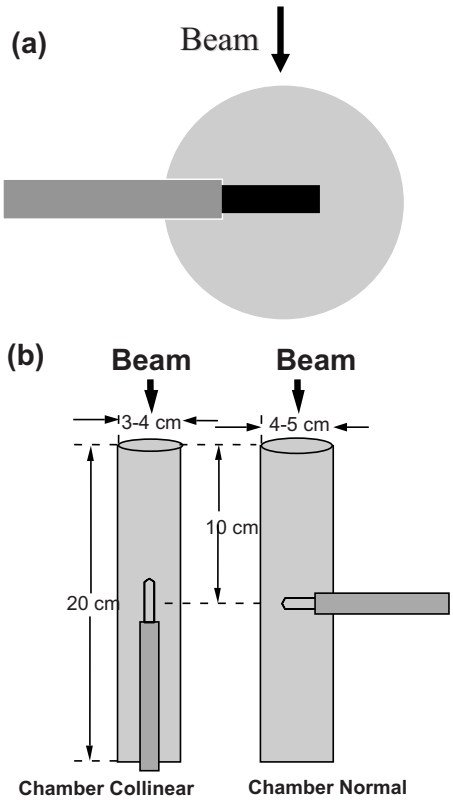

FIG. 7. (a) An example of an old style S_c measurement using a peak thickness build-up cap. Such measurments allowed charged particle contamination to affect the readings inappropriately. (b) Miniphantom as described by van Gasteren.

detailed measurements of the x-ray source distribution of a linear accelerator. The cumulative source distribution of a linear accelerator was measured in terms of focal and extrafocal components using secondary collimation techniques, as depicted schematically in Fig. 3.

In practice, information about the source size is often inferred from the penumbra width and shape. Studies also correlate the value of S_c at small field sizes with the penumbra width produced by an accelerator.[102]

V. MEASUREMENT OF IN-AIR OUTPUT RATIO

This section deals with the experimental methods used to measure in-air output ratio and the correction formalism one can use to correct for artifacts caused by miniphantoms made of different materials.

V.A. Influence of build-up material and detectors

V.A.1. Measurement of the effect of miniphantom on S_c

V.A.1.a. Conventional build-up cap measurements. The original in-air measurements to determine S_c used build-up caps [Fig. 7(a)] to bring the thickness of detector walls to provide equilibrium. While ^{60}Co gamma rays require build-up caps of approximately 0.5 g cm^{-2} in mass thickness, when extended to higher energies the diameter of the cap may became impractically large. While full build-up thickness is commonly interpreted to equate with d_{max} for the photon component of the beam, the thickness required to eliminate electron contamination is often larger than d_{max}.[104] Thus, the use of build-up caps with a thickness just equal to d_{max} may allow charged particle contamination radiation to reach the detection volume, erroneously increasing the reading particularly for the larger field sizes. Frye *et al.*[104] and Venselarr *et al.*[105] showed that the field size dependence of S_c is affected by electron contamination if the cap thickness is not sufficient.

For the measurement signal to scale with the kerma of incident radiation, lateral electron equilibrium conditions must be established, and the full cap must be exposed to the radiation beam, limiting the minimum beam size to the cap diameter plus a margin to account for penumbra. To enable the use for smaller fields, higher Z materials have been used, such as lead.[100] However, it has been argued that the high-Z materials may alter beam spectra and thus introduce errors.[12,106] Several investigators studied the influence of build-up cap material on the measurement of S_c.[104,107,108] Frye *et al.*[104] reported significant differences (up to 4.8% for a 24 MV beam) between the measurements with conventional build-up caps made of Solid Water and those with graphite. Using a magnetic field to sweep the contaminant electrons in the 24 MV beam, they concluded that a significant portion of the difference was indeed from the charged particle contamination. With build-up caps made of low- and high-Z materials, Jursinic and Thomadsen[107] found large difference (up to 4%) for an 18 MV beam, especially for large field sizes. These increased differences are most likely due to the contributions from contaminating electrons, as the longitudinal thicknesses of their caps were no more than the maximum dose build-up depths. Thomadsen *et al.*[103] reported that electron contamination penetrates considerably farther than the depth of maximum dose, and for the 24 MV beam, some contamination reaches as much as 10 cm depth.

This report does not provide a solution for situation when the historically used "collimator-scatter factor" measured at d_{max} is used for TMR-based MU calculation algorithm. In this case, we recommend using S_c (in air output ratio) defined at 10 cm (see below for van Gasteren miniphantom) so long as $S_p = S_{cp}/S_c$ is determined using S_{cp} measured at d_{max}. A brief description of the rationale why this approach will improve MU calculation accuracy, which is an expansion of the argument made by Ten Haken,[109] is included as follows: We will consider the common situation where the dose to be determined is for a point at the isocenter at a depth d (d is much deeper than the range of contamination electrons) with field size s and collimator setting c. The collimator setting c is, in general, greater than or equal to the field size s. If we reduce the collimator setting for the moment to a new value c' such that $c' = s$, then the dose can be determined by multiplying the dose at the reference configuration by S_{cp} for the change in the field size and then multiplying by TMR for the change in depth. When $c' = s$, S_{cp} and TMR are measured under the same conditions (d_{max}) as that of the calculation so that the calculation is as accurate as the measured data. When the collimator setting is increased back to c from c',

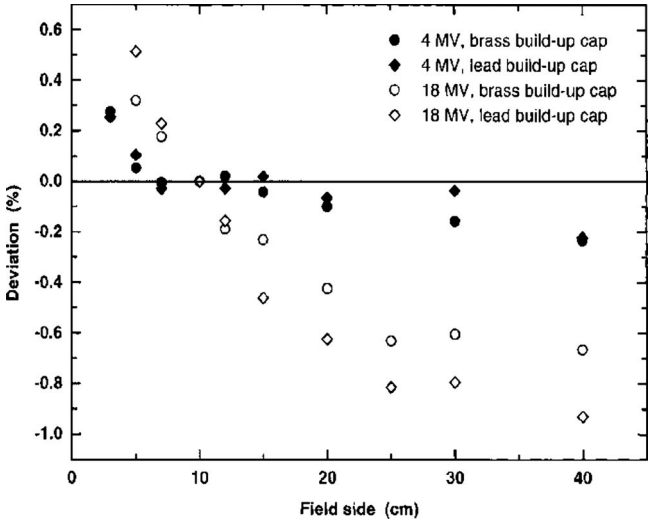

FIG. 8. Deviation in the result of S_c measurement caused by using high-Z material, relative to that using water-equivalent miniphantom. [Taken from Weber *et al.* (Ref. 108)].

the increase in dose is represented by a factor $S_c(c)/S_c(c')$. Since the calculation point is at the depth d without contaminating electrons, the S_c measured with miniphantom should be used for this factor instead of the S_c measured at d_{max}. Thus, as long as the depth of calculation is beyond the range of contaminating electrons, the S_c measured with the miniphantom should be used whether one uses TMR or TPR. When the depth of calculation is shallow, the contribution from electron contamination is included in $S_p(s)$ and $S_c(c)$ for the TMR-based formalism, depending on whether S_c is measured at depth beyond electron contamination or d_{max}. The equivalent square dependence for photon phantom scatter, s, and that for the headscatter, c, do not strictly apply in either cases for $S_p(s)$ and $S_c(c)$ due to the additional field size dependence caused by electron contamination. In this case, neither method provides a satisfactory solution when c and s is very different.

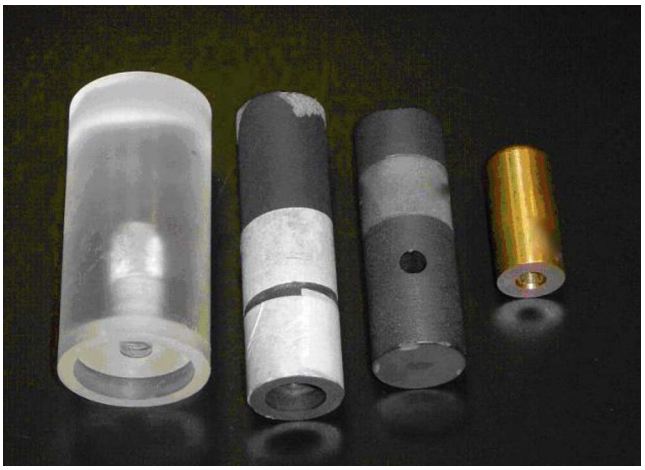

FIG. 9. Recommended miniphantoms for measurement of S_c. The material compositions are, from left to right, Lucite, graphite, and brass. If a high-Z miniphantom is chosen, a correction factor may be required.

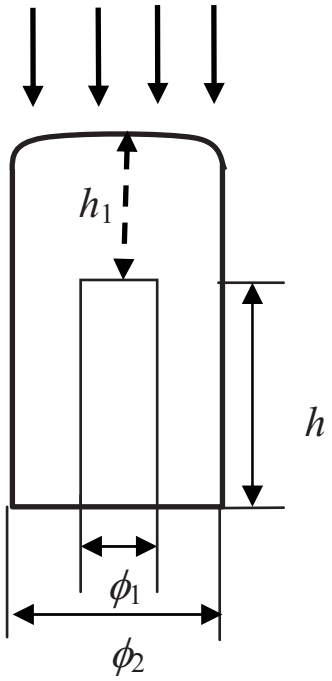

FIG. 10. Schematics of a brass miniphantom recommended for measurements of S_c for square fields larger than 1.5×1.5 cm^2 and photon energy less than 25 MV. The longitudinal thickness (h_l) of the miniphantom facing the radiation should equal to or be larger than 1.2 cm (or 10 g/cm^2, $\rho=8.4-8.7$ g/cm^3). The inner diameter of the miniphantom, ϕ_1 equals to the outer diameter of the detector, e.g., 0.6 cm. The height, h, should be sufficient long to cover the detector sensitive volume, e.g., 2 cm. The outer diameter of the miniphantom, ϕ_2, can be such that the wall is thinner [but minimum 1.2 mm brass for up to 18 MV (Refs. 107 and 115)] than the thickness required for CPE given that the total lateral dimension above the chamber well ensures lateral CPE for the photon energy, and the effect on S_c measurement falls within required accuracy demands.

V.A.1.b. van Gasteren miniphantom measurements. It can be concluded, based on the studies above, that one of the most important factors in the measurement of S_c is to ensure that the cap's longitudinal dimension is sufficient to prevent contaminating electrons from reaching the detector. van Gasteren *et al.*[12] showed that once the water-equivalent cap, or "miniphantom," is thick enough, S_c can be measured reliably. They proposed the use of a columnar, cylindrical miniphantom, 20 cm long$\times4-5$ g cm^{-2} in diameter, oriented coaxially with the chamber and beam [see Fig. 7(b)].[12] The minimum lateral dimension (or diameter) must exceed 4 g cm^{-2} (for up to 24 MV photons) to reach lateral electron equilibrium.[110] The radiation field edges must exceed the miniphantom lateral dimension to maintain the cap in the uniform part of the radiation field (keeping the penumbra from impinging on the miniphantom). This requirement ensures that the phantom-scatter contribution generated by the miniphantom for the actual and the reference collimator settings would mutually cancel (see Sec. II B). We endorse this cylindrical columnar miniphantom for the range of fields it can accommodate; however, for output ratio measurements for small fields common in IMRT treatment, we instead recommend using higher mass density material with medium Z (see Figs. 9 and 10).

Choices of phantom materials affect the results with the van Gasteren-style miniphantoms. Miniphantoms made of low-Z materials are generally recommended. To extend the range of S_c to smaller field sizes, one approach has been to use higher density, higher atomic number miniphantoms. Li *et al.*[110] compared the measurements using cylindrical miniphantoms made of polystyrene and brass. Their data show that as long as the longitudinal dimension of miniphantom is sufficient to prevent contaminating electrons from reaching the detector, the measurements with polystyrene and brass miniphantoms agree within 0.5% for both 6 and 18 MV beams. However, even if the thicknesses of a miniphantom is sufficient to stop contaminating electrons, the use of a lead phantom may result in errors in the values of S_c of up to $\pm 1\%$. By comparing measurements with build-up caps made of low- and high-Z materials (carbon for low Z, brass and lead for high Z), Weber *et al.*[108] observed deviations of up to $\pm 1\%$ in the S_c values for high-energy beams (see Fig. 8). They reported that the thicknesses of their build-up caps were sufficient to stop contaminating electrons. The magnitude of errors caused by high-Z material increases with collimator setting, being small for collimator settings less than 6×6 cm^2, but rising to the 1% level for a 40×40 cm^2 field for lead. For lead and acrylic miniphantoms, no differences were found for small collimator settings.[100] When using miniphantoms of a high-Z material, the methodology in Sec. V C of this report is recommended.

V.A.2. Monte Carlo simulation of the effect of miniphantom on S_c

At the time of this report, the task group is not aware of any literature that addresses the Monte Carlo simulation of miniphantom for investigation of S_c. Johnsson and Ceberg performed a Monte Carlo study on the effect of water-equivalent miniphantom's longitudinal thickness on the accuracy of transmission measurement.[111] They defined a measurable quantity as the "collision kerma in-water" at a point in free space, similar to the definition of the in-air output function, O_{air}. When the ionization ratio measured in a miniphantom equals the collision water kerma ratio in the free space, the condition is called *in-air equivalent*.[111] They reported a range of miniphantom depths for specific photon energy in order to obtain accurate measurement of transmission to within 1% (or in-air equivalent) in a water-equivalent miniphantom. However, the limit of phantom thickness on S_c is likely to be much relaxed because the photon energy spectra do not change as much as that for the transmission measurements. Experimental studies have shown no effect of phantom's longitudinal thickness on S_c as long as the thickness is sufficient for CPE.[12] Tonkopi *et al.*[112] performed MC simulation for OAR measurement and showed that using a plastic miniphantom gives more accurate air-kerma profile measurement than using high-Z material build-up caps.

V.A.3. Influence of detectors on measurement of S_c

Various detectors (e.g., ionization chamber and diode) have been used to measure S_c. Values of S_c measured with diode detectors, shielded or unshielded, are identical to those from ionization chamber measurements.[113] It is also reported that the ionization chamber orientation (whether its axis is perpendicular or parallel to incident radiation) does not affect the measured results.[70,107] However, for very small field size, the detector sensitive volume will have a drastic effect on measured value of S_c.[114] Thus it is important to choose detectors with small sensitive volume for collimator setting less than 1×1 cm^2.

V.B. Development of correction factors for high accuracy applications

An important aspect of the unambiguous formal definition of S_c given by Eq. (3) is that build-up cap and detector combinations of practical interest can be Monte Carlo simulated or modeled by means of cavity theory to fully quantify correction factors for high accuracy applications.[14,115] The ratio of readings for an S_c measurement can, by assuming equilibrium conditions and a detector fulfilling the Bragg–Gray cavity criteria, be expressed with a more general formulation than used in Eq. (6) to yield

$$\begin{aligned}\frac{X(c)}{X(c_{\mathrm{ref}})} &= \frac{\Psi(\mu_{\mathrm{en}}/\rho)}{[\Psi(\mu_{\mathrm{en}}/\rho)]_{\mathrm{ref}}}\cdot\frac{\mathrm{SF}_K(c)}{\mathrm{SF}_K(c_{\mathrm{ref}})}\cdot\frac{s^{\mathrm{S\text{-}A}}_{\mathrm{det,med}}}{[s^{\mathrm{S\text{-}A}}_{\mathrm{det,med}}]_{\mathrm{ref}}}\cdot\frac{\beta}{\beta_{\mathrm{ref}}}\cdot e^{-(\bar{\mu}-\bar{\mu}_{\mathrm{ref}})d}\\ &= S_c\frac{(\mu_{\mathrm{en}}/\rho)^{\mathrm{med}}_{\mathrm{wat}}}{[(\mu_{\mathrm{en}}/\rho)^{\mathrm{med}}_{\mathrm{wat}}]_{\mathrm{ref}}}\cdot\frac{\mathrm{SF}_K(c)}{\mathrm{SF}_K(c_{\mathrm{ref}})}\cdot\frac{s^{\mathrm{S\text{-}A}}_{\mathrm{det,med}}}{[s^{\mathrm{S\text{-}A}}_{\mathrm{det,med}}]_{\mathrm{ref}}}\cdot\frac{\beta}{\beta_{\mathrm{ref}}}\\ &\quad\times e^{-(\bar{\mu}-\bar{\mu}_{\mathrm{ref}})d}, \qquad (30)\end{aligned}$$

where S_c is defined in Eq. (3), Ψ is the energy fluence free in air, $(\bar{\mu}_{\mathrm{en}}/\rho)$ is the mean (energy fluence weighted) mass energy transfer coefficient for the miniphantom material, $\mathrm{SF}_K = K/K_p$ is the total-to-primary kerma ratio (or kerma scatter factor) that accounts for miniphantom scatter, $S^{\mathrm{S\text{-}A}}_{\mathrm{det,med}}$ is the mean (secondary electron fluence weighted) Spencer–Attix stopping power ratio of electrons between the detector and the miniphantom medium for the detectors sensitive volume,[116] d is the effective depth of the detector, $\bar{\mu}$ is the mean attenuation coefficient (energy fluence weighted), β is the dose-to-collision kerma ratio, $(\bar{\mu}_{\mathrm{en}}/\rho)^{\mathrm{med}}_{\mathrm{wat}}$ is the mass energy transfer coefficient ratio for the miniphantom material and water, and the variables with a subscript "ref" denotes the corresponding variables for the reference geometry. Correction factors can be used to mitigate eventual spectral/material induced shifts caused by measurement technique as to convert the reading from the measurement geometry to the "water kerma in free-space" conditions of definition for S_c. For example, from Eq. (30) we can derive

$$S_c = \frac{X(c)}{X(c_{\mathrm{ref}})}\cdot \mathrm{CF}_{\mathrm{en}}\cdot \mathrm{CF}_{\mathrm{SF}}\cdot \mathrm{CF}_S\cdot \mathrm{CF}_{\mathrm{att}}\cdot \mathrm{CF}_\beta, \qquad (31)$$

where $\mathrm{CF}_{\mathrm{en}} = (\bar{\mu}_{\mathrm{en}}/\rho)^{\mathrm{med}}_{\mathrm{wat,ref}}/(\bar{\mu}_{\mathrm{en}}/\rho)^{\mathrm{med}}_{\mathrm{wat}}$ corrects for energy transfer shifts, $\mathrm{CF}_{\mathrm{SF}} = \mathrm{SF}_{K,\mathrm{ref}}/\mathrm{SF}_K$ corrects for miniphantom scatter factor differences, $\mathrm{CF}_S = [S^{\mathrm{S\text{-}A}}_{\mathrm{det,med}}]_{\mathrm{ref}}/S^{\mathrm{S\text{-}A}}_{\mathrm{det,med}}$ corrects for stopping power differences,[117] $\mathrm{CF}_\beta = \beta_{\mathrm{ref}}/\beta$ corrects for

electron equilibrium, and $CF_{att}=e^{(\bar{\mu}-\bar{\mu}_{ref})d}$ is to cancel out attenuation differences. All these correction factors can be a function of collimator setting, energy, and miniphantom geometry and material. For miniphantoms made with sufficient thickness, $CF_{\beta}=1$. The shift of stopping power ratio at different depth d and collimator setting c is usually negligible for an open beam: $CF_S=1$.[117] The values of various correction factors for S_c determination have been evaluated in several recent publications.[14,115] For example, for a water-equivalent miniphantom the total correction factor remains indistinguishable from unity, while for a miniphantom made of lead, the total correction factor with thickness of 21.6 g cm^{-2} is up to $\pm 1\%$.[14,115]

V.C. Recommendation of miniphantom dimension for S_c

For most field sizes, S_c measurements should be made with the detector in a miniphantom, as shown in Fig. 9. The miniphantom should be made from water-equivalent materials, such as solid water, acrylic (PMMA), or graphite, with 4 g/cm^2 diameter and with the detector at 10 g/cm^2 depth, as described by van Gasteren *et al.*[12] and the ESTRO protocol.[1] For small collimator settings ($c<5$ cm), a miniphantom made of high-Z material (e.g., brass or lead) must be used to ensure CPE and contaminant electron filtering, and the procedure for their use is given below. Measurement at extended SSD for small fields may result in different S_c because of the different projections of the x-ray source from the detector point of view. Such measurements should be avoided as discussed in the next section. The lateral dimension (diameter) of the miniphantom should be sufficiently large to maintain lateral CPE.[110] Thinner lateral wall thickness[107] may be used if experimental verification show that the effect on S_c measurement falls within the user's desired accuracy. The height above the detector should be sufficient (10 g/cm^2) to not only maintain longitudinal CPE but also to eliminate contaminant electrons. The detector and miniphantom should be supported on a low density stand (e.g., Styrofoam) to minimize additional scatter into the detector volume.

To provide lateral CPE for the small segment fields that are common in IMRT, a high-density miniphantom shall be used to enable full beam coverage of a phantom providing enough filtering and buildup. Jursinic *et al.*[107,115] showed that a water-equivalent wall thickness of 1 g cm^{-2} (about half of MC predicted lateral CPE range) is sufficient to measure changes in S_c data to within an uncertainty of 0.3% for open beams. Brass (approximately 63% Cu, 37% Zn) is an acceptable alloy compromising high density (8.4 g cm^{-3}) with moderate atomic numbers (29 and 30), good machinability and well known dosimetric properties.[108,110,118] Figure 10 shows the schematics of a brass miniphantom suitable for measurement of small field sizes. However, the introduction of high-Z material changes the response and the use of correction factors calculated by Eqs. (30) and (31) is preferred, when available.

A recommended method to determine S_c is as follows: For field sizes larger than 5×5 cm^2, use a water-equivalent miniphantom; for field sizes below 5×5 cm^2, use a high-density (and thus high-Z) miniphantom, allowing extension to field sizes for which the diameter of the high-density miniphantom is completely within the field, including the penumbral margins. The ratio obtained with the high-density miniphantom does not give the correct values for S_c but normalizing the results obtained with the high-density miniphantom to a 5×5 cm^2 field and multiplying the resultant values by the S_c measured for a 5×5 cm^2 field with a water-equivalent miniphantom gives values with very little error.

V.D. Measurement of S_c for small field sizes

For IMRT and stereotactic radiotherapy, it is often desirable to measure S_c for small field sizes (c less than 3×3 cm^2). For these field sizes, the primary cause of variations in S_c is the direct source-obscuring effect, as discussed in Sec. IV F. We recommend measuring S_c at the distance of interest, usually at the isocenter plane (SAD = 100 cm) following the procedure in Sec. V C. To ensure that the miniphantom is completely covered within the small field, a high-Z material miniphantom such as the one described in Fig. 10 can be used. This one is suitable for measurement of field sizes down to 1.2 cm. Several studies has found that there is no Z dependence of phantom materials for small field sizes.[14,100,119] A recent study suggested one can obtain reliable data using a miniphantom of zero side wall thickness for photon energy up to 6 MV.[114] However, for source size less than 1 cm diameter (e.g., 0.5 cm stereotactic cone), the averaging effect of the active volume of the detector becomes more important than the miniphantom lateral dimension.[114] Thus it is recommended that measurement for field size less than 1×1 cm^2 be avoided unless cares are taken to account for the detector convolution effect.[114]

Measurement at large extended SSD (e.g., SSD ~400 cm) is not recommended for use at the isocenter because of the different projections of the x-ray source from the detector point of view. Further studies are necessary to convert the S_c measured at different SSDs for small field sizes. Several groups have made measurements of S_c at extended SSD to study the x-ray source size distribution because the radiation beam becomes almost parallel.[11,64,100]

VI. EMPIRICAL METHODS FOR CHARACTERIZATION OF S_c

VI.A. Empirical modeling of multiple photon sources and monitor backscattering

The collimator exchange effect described the fact that the in-air output ratio differs for a rectangular radiation field depending on which side of the rectangle delineates the inner and outer collimator jaws (i.e., $c_x\times c_y$ or $c_y\times c_x$).[120] It can be explained by the varying view of the flattening filter at the point of detector (Fig. 3). An equivalent square formula can be used to characterize this effect,[121]

$$c = (1+k)\cdot c_y \cdot c_x/(k\cdot c_x + c_y). \tag{32}$$

Here c_x and c_y denote the settings of the outer and inner collimators, respectively, and k (>1) is the collimator exchange coefficient. If only the headscattered photons are considered, then k can be determined from the head geometry as.[122]

$$k = z_x \cdot (\mathrm{SDD} - z_y)/z_y \cdot (\mathrm{SDD} - z_x), \tag{33}$$

where z_x and z_y are the source-to-collimator distances for outer and inner collimators and SDD is the source-to-detector distance (see Fig. 1). The value of k has been determined experimentally for the Elekta[121] and Varian[122] accelerators (k=1.8). However, k for a particular make/model of accelerator may be different from this value and varies between 1.2 and 1.8 for the major accelerator types.[123] Table V in Appendix A gives examples of S_c for rectangular fields to illustrate the collimator exchange effect. Other formalisms ($k=z_x/z_y$) have also been proposed to calculate S_c for rectangular fields.[124] The source-obscuration effect is only relevant for very small collimator settings (usually less than 2 $\times 2$ cm^2), then it becomes the dominating effect and reduces the in-air output ratio to zero when the collimators are closed. It has been described by Zhu *et al.*[100,102]

The monitor-backscatter effect differs for different accelerator models and can be measured by operating the accelerator without the dose-rate servo control,[94] by using a "telescope" method,[91,93,90] by target-current pulse counting,[93] by using the target charge method,[93] or by photoactivation of copper placed above the flattening filter.[60] The first two methods do not require opening up the accelerator head or special electronic instruments and can achieve a reproducibility of 0.3%, but are still very time consuming. For some Varian accelerators, the maximum contribution from the monitor backscatter can be large (3%–5%).[91] In principle, the monitor backscatter factor could be defined as $S_b=(1+b(c_{\mathrm{ref}}))/(1+b(c))$ implementing Eq. (29) as

$$b(c_{x1},c_{x2},c_{y1},c_{y2}) \approx \frac{k_b \cdot z_{\mathrm{SMD}}^2}{\pi \cdot 100^2}\left[\frac{40(40-c_y)}{(z_y - z_{\mathrm{SMD}})^2} - \frac{c_y \cdot (40-c_x)}{(z_x - z_{\mathrm{SMD}})^2}\right], \tag{34}$$

where we have neglected the cosine factor in the integrand of Eq. (29) and have made further assumption that the maximum irradiated area is 40×40 cm^2, projected at the isocenter. The distances (z_x, z_y, and z_{SMD}) are shown in Fig. 1, and $c_x=c_{x1}+c_{x2}$ and $c_y=c_{y1}+c_{y2}$ are the collimator settings of the independent jaws. (Y jaws are always defined as the inner collimator jaws and X jaws are always the outer collimator jaws.) Clearly, the monitor backscatter factor increases with increasing collimator settings and Y-jaw setting is dominant since $z_y<z_x$. The backscatter can also be characterized by separating the in-air output ratio S_c into a multiplication of S_b and S_h [see Eq. (27)], where

$$S_b = \frac{1+b(c_{\mathrm{ref}})}{1+b(c)} \approx 1 + \frac{k_b \cdot s_M^2}{\pi \cdot 100^2}\left[\frac{40(c_y - c_{\mathrm{ref}})}{(z_y - z_{\mathrm{SMD}})^2} - \frac{c_x c_y - c_{\mathrm{ref}}^2 - 40(c_y - c_{\mathrm{ref}})}{(z_x - z_{\mathrm{SMD}})^2}\right]. \tag{35}$$

We have used expression Eq. (34) for b and assume that $b \ll 1$.

Several headscatter models have been successfully used to predict S_c on the central axis. These models use a set of measurements from square collimator settings to extract the necessary parameter. One example of such model uses three parameters (a_1, a_2, and λ) to calculate S_c. a_1 is the monitor-backscatter coefficient, a_2 is the maximum scatter-to-primary ratio, i.e., if a_2=0.10, 10% of the incident fluence is indirect radiation, and λ is the width of the indirect radiation distribution at the isocenter plane. The in-air output ratio on the central axis is[123]

$$S_c(c) = \frac{(1+a_1\cdot c)\cdot(1+\mathrm{SPR}_{\mathrm{air}}(c))}{(1+a_1\cdot 10)\cdot(1+\mathrm{SPR}_{\mathrm{air}}(10))} = (1+a_1\cdot c)(1+a_2\,\mathrm{erf}(c/\lambda)^2)\cdot H_0, \tag{36}$$

where H_0 is a normalization constant that sets $S_c=1$ at the collimator setting 10×10 cm^2 and $\mathrm{SPR}_{\mathrm{air}}(c)=a_2\,\mathrm{erf}(c/\lambda)^2$ is the scatter-to-primary ratio for the headscatter component compared to the primary component, and $\mathrm{erf}(x)=\int_0^x e^{-t^2}dt$ is the error function. c is the equivalent square calculated from the collimator jaws using Eq. (32) for rectangular fields. The incident kerma measured in the miniphantom is separated into the direct K_d and the indirect (or headscatter) K_h components such that $K_{\mathrm{air}}=K_d+K_h=K_d\cdot(1+\mathrm{SPR}_{\mathrm{air}})$. Details of the derivation can be found elsewhere.[123] Typical parameters for a range of linear accelerators can be found in Table II.

Equation (36) can also be used to model $S_{c,w}$ for a wedged beam.[123] (Some representative data are shown in Table IV.) However, it is better to separate the headscatter components from the wedge and the flattening filter. Zhu *et al.*[75] provided some empirical expressions to model the headscatter from internal and external wedges appropriately (see Fig. 11). $\mathrm{SPR}_{\mathrm{air},w}$ is the ratio of headscatter-to-direct radiation for the wedge,

$$\mathrm{SPR}_{\mathrm{air},w}(c) = \begin{cases} \gamma_w\,\mathrm{erf}(c/\lambda_w)^2 & \text{(internal wedge)} \\ \alpha_w\cdot(c/40)^2 & \text{(external wedge)}, \end{cases} \tag{37}$$

where γ_w, α_w, and λ_w are constant parameters. The parameter γ_w (or α_w) determines the maximum SPR for the largest field (40×40 cm^2) and can be obtained by least squares fitting to the square field S_c data for wedged beams.[75]

VI.B. S_c for MLC shaped fields

The use of an MLC for field shaping does not change the way the phantom scatter is computed. The in-phantom scatter depends on the final field size projected on the patient and the methods for calculating scatter dose in the patient are

TABLE II. Parametrization (a_1, a_2, and λ) of open, square field from different accelerators for Eq. (36). Taken from Zhu *et al.* (Ref. 123).

Model	Energy (MeV)	a_1 (cm^{-1})	a_2	λ (cm)	Max deviation (%)	Std deviation (%)
Varian 2300CD	6	0.0015	0.064	8.12	0.4	0.3
	15	0.0014	0.050	8.45	0.4	0.2
Varian 2100CS	6	0.0013	0.066	8.74	0.1	0.1
	10	0.0014	0.076	8.47	0.2	0.1
Varian 2100CD/MLC	6	0.0013	0.067	8.06	0.4	0.2
	15	0.0012	0.051	7.47	0.3	0.2
Varian Clinac 1800	6	0.0009	0.072	7.96	0.1	0.1
	18	0.0010	0.074	8.11	0.2	0.1
Varian Clinac 6/100	6	0.0008	0.066	8.47	0.5	0.3
Varian Clinac 600C	6	0.0005	0.053	8.80	0.3	0.2
Elekta SL75/5 #1	6	0.0008	0.059	7.52	0.4	0.2
Elekta SL75/5 #2	6	0.0007	0.061	7.81	0.6	0.4
Elekta SL20	6	0.0005	0.081	9.99	0.6	0.3
	20	0.0008	0.119	8.48	0.3	0.2
Elekta SL25/MLC	6	0.0003	0.069	10.8	0.6	0.4
	25	0.0007	0.104	7.64	0.8	0.5
Elekta SL25	6	0.0007	0.066	9.31	0.4	0.2
	25	0.0007	0.102	7.77	0.6	0.4
Siemens Primus	6	0.0004	0.099	9.15	0.5	0.3
	18	0.0006	0.115	7.95	0.9	0.4
Siemens KD2	6	0.0004	0.079	9.69	0.4	0.2
	15	0.0004	0.088	9.19	0.3	0.2
Siemens MXE	6	0.0005	0.117	8.21	0.8	0.3
Cobalt T-1000	1.25	0.0012	0.086	14.2	0.4	0.2

well established. However, the in-air output ratio for MLC shaped fields is dependent on the design and the geometry of the MLC system. The amount of scatter radiation reaching a point downstream from a MLC system depends on the area of the extrafocal radiation source as seen by the point through different levels of collimators. If the MLC is located at the position of the inner jaws in the secondary collimator, as in the Elekta MLC design, the irregular field shape determines both the headscatter and the phantom scatter. In the Elekta design, there is a pair of backup jaws situated under the MLC leaves and motorized to travel in the same direction as the leaves. These backup jaws serve to minimize the interleaf transmission outside the radiation field. These jaws are normally set at the same position as the outermost leaves and make only a small contribution to the headscatter. Palta *et al.*[125] showed that the in-air output ratio for shaped fields with Elekta MLC can be accurately calculated using an equivalent square[126] of the MLC shaped field. The equivalent square for the MLC shaped field can be readily calculated using Clarkson sector integration method[127] if it is assumed that the source of extrafocal radiation is radially symmetric. It is important to note that the integration method is valid only when the field dimensions in both the measurements and the calculations are projected from the calculation point back through the collimation system to the effective source plane of extrafocal radiation.[129] If the MLC replaces the outer jaws in the secondary collimator, as in the MLC design of Siemens, both the MLC leaf positions and the upper jaw positions determine the in-air output ratio. Since the jaws are closer to the effective collimator-scatter source, they define the field aperture in the dimension perpendicular to the direction of leaf travel in both the BEV and in the projection of the calculation points. When the MLC is used as a tertiary collimator along with the inner and the outer collimator, as in the design of Varian, the field shape defined by the MLC is closer to the plane of any given calculation point than the inner or outer jaws. Unless the MLC shaped field is substantially smaller than the rectangular field formed by the inner and outer collimator jaws, the tertiary blocking boundary will not affect the projection of the field size from the calculation point back to the effective source of extrafocal radiation. In this case, the jaw openings determine the in-air output ratio.[128] However, Kim *et al.*[4] showed that the scatter radiation contribution from the tertiary MLC to the in-air output ratio for small MLC shaped fields may not be negligible. This is often the case in small beam apertures used for intensity modulation.

Zhu *et al.* developed an algorithm to calculate S_c based on an empirical model[123] by projecting each leaf position to the isocenter plane,[68]

$$S_c = (1 + a_1 \cdot c) \cdot \left(1 + a_2 \cdot \frac{1}{\pi(\lambda/2)^2} \int\int e^{-r^2/(\lambda/2)^2} dA\right) \cdot H_0, \tag{38}$$

where $\lambda/2$ is the effective radius of the extended source of photons scattered from the flattening filter projected on the

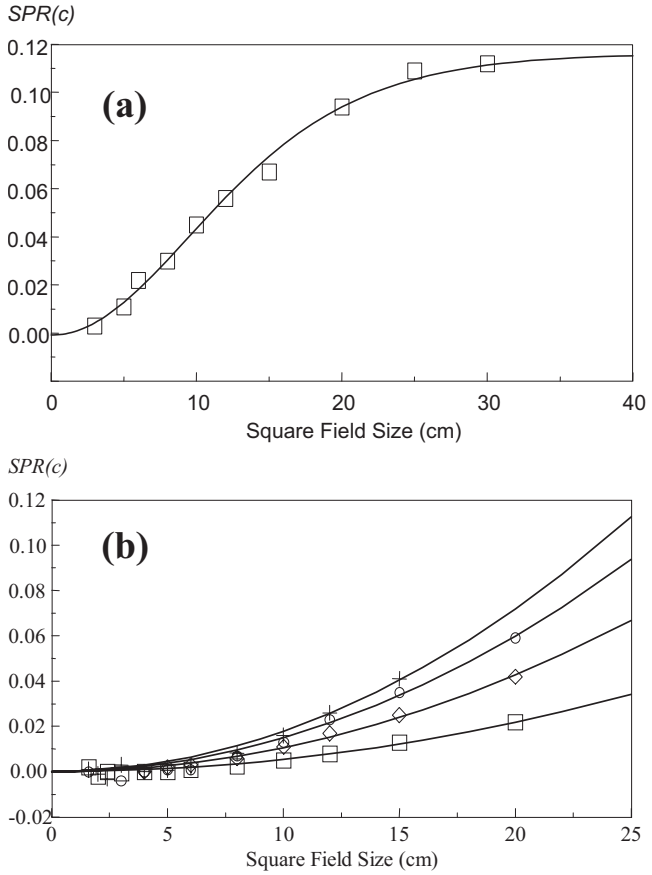

FIG. 11. The field size dependence of the ratio of headscatter-to-direct radiations on the central axis for (a) the internal wedge of SL75-5 and (b) the external wedge of a Varian 2100C. Taken from Zhu *et al.* (Ref. 75).

isocenter plane and H_0 is an normalization factor to make $S_c=1$ for a 10×10 cm^2 field. The integral extend to infinite on the isocenter plane. This formula does not require the exact knowledge of the head geometry. λ, a_1, and a_2 can be determined from least squares fitting the measured S_c to Eq. (36) for square field sizes on the central axis. The integral can be calculated analytically for a known MLC leaf pattern. The calculation agrees with measurement to within 1.2% for points both on and off the central axis and is better than the equivalent square method. The fitting parameters used in the algorithm are derived from measurements for square field sizes on the central axis. Zhu *et al.*[68] compared the results for the three types of MLC mentioned above and found that for the same MLC shaped irregular field, the value of S_c increases from the Elekta, to the Siemens, to the Varian accelerators, with differences up to 4%. When the MLC leaf positions are substantially different from the secondary collimators (or the rectangular field encompassing the irregular field), one observes differences up to 5% in the value of headscatter correction factor (HCF) defined as the ratio of in air output ratio between the MLC shaped irregular field and that of the rectangular field encompassing the irregular field.

VI.C. S_c for dynamic wedge and IMRT

VI.C.1. Dynamic wedge

The dynamic wedge (DW) makes use of movement of one pair of independent linac collimators closing (or opening) during the treatment delivery to produce a wedge-shaped profile. This offers flexibility in creating wedge-shaped dose distributions. As an example, the Varian DW is implemented using so-called "segmented treatment tables" (STTs) that control the dose rate and collimator movement for producing the dynamic wedges. Each STT contains information on the moving collimator position versus cumulative weighting of the monitor units. There are a total of 132 STT for four wedge angles (15°, 30°, 45°, and 60°).

The second generation of dynamic wedge, called the enhanced dynamic wedge (EDW), became available later on Varian linacs. EDW uses a single STT to generate all the other STTs for all field sizes and wedge angles.

It has been reported that the $S_{c,w}$ values for the dynamic wedge are significantly different from that for the open[129,130] or physically wedged[58] field. This difference is primarily because of the change in scattering conditions as the dynamic collimator jaw moves. In order to characterize this difference, Liu *et al.*[129,130] proposed that the S_c for dynamic wedge may be expressed as: $S_{c,w}=S_{c,n}\cdot N(c_y)$, where $N(c_y)$ is the ratio of the STT weights on the central axis between the field of interest (c_y) and the reference field ($c_y=10$ cm),

$$N(c_y)=\frac{\mathrm{STT}(c_y,y_i=0)}{\mathrm{STT}(c_y=10,y_i=0)}. \tag{39}$$

Here, c_y is the field width in the wedge direction and y_i is the distance between the central axis and the moving jaw edge, so $y_i=0$ represents the position of the moving jaw at the collimator axis. The $S_{c,n}$ values were found to be approximately the same as the S_c values for the open fields.[129,130] The introduction of $S_{c,n}$ and $N(c_y)$ simplifies the determination of S_c for dynamic wedge. The quantity $N(c_y)$ characterizes the impact of dynamic wedge on S_c and varies between 0.4 and 1 for c_y varying between 10 and -10 cm. As noted previously, $S_{c,w}$ for wedged beam is often not used in conventional MU calculation algorithms, where S_c for open beam alone is used, and the headscatters from wedge fields are lumped into the field size dependent wedge factors. Users are cautioned to avoid double counting the in-air output ratio if a field size dependent wedge factor is used.

VI.C.2. IMRT

There is, in principle, no difference between calculation of S_c for an IMRT field and calculation of S_c for an open field since the former is simply an MU-weighted summation of the latter, particularly, a summation of a series of MLC shaped fields. However, it is more demanding in terms of the accuracy required to determine S_c for each segment of an IMRT field. One has to determine S_c for points not only inside of the beam collimation but also outside the beam collimation (under the blocks).

Efforts to address the prediction of S_c for IMRT segments have been made by several groups.[68,131–134] Hounsell and Wilkinson[135] proposed a simple method, a first-order Compton scatter approximation from the flattening filter, which only considers scatter from the flattening filter. The calculation of S_c using this method was found to agree with the measurements only at small field sizes (between 2×2 and 10×10 cm^2).[135] Naqvi *et al.*[134] used a two-source model combined with raytracing algorithm to calculate the headscatters for IMRT fields. Their data indicated that the potential accumulative errors in S_c on the order of a few percent could be avoided with the use of this model. Yang *et al.*[133] proposed a three-source model to calculate the headscatter distribution for irregular segments shaped by MLC. In this model, the values of S_c for each beamet in a segment at the point of calculation are considered to be contributed from three sources: Primary photons and scattered photons from primary collimators or flattening filter. S_c predicted by this model agreed with the measurement within $\pm 3\%$ at an any calculation point.[133] Recently, Zhu *et al.*[68] calculated S_c for an MLC field using an empirical algorithm that projects each leaf position to the isocenter plane. Their calculation showed that S_c for an irregular MLC field can be different by as much as 5% from the S_c for the rectangular field encompassing the irregular field.

VII. QUALITY ASSURANCE

As outlined in AAPM Task Group Report 40,[136] QA, in general, has a critical role in all aspects of radiation oncology. The quality of S_c data is important for accuracy of dose calculations in both treatment planning systems and MU calculations. QA of S_c is needed (i) at the time of beam commissioning, (ii) for periodic (yearly) checks, (iii) after any major repair of the linac, and (iv) at the time of upgrade of treatment planning software. This section will discuss various QA methods existing in literature for S_c data. That includes, primarily four categories of methods: (a) Use of linac specific published data, (b) use of published parameterized values, (c) use of the in-water output ratios divided by published phantom scatter factors, and (d) remeasurement.

A database of measured values, for open and wedged fields of major linac models and cobalt units, exists in literature.[123] Tables III and IV provide open and wedged-field data measured by some of the authors of this report on select linacs. To emphasize the impact of linac head design, the data include linacs from three major vendors: Varian, Siemens, and Eleckta. For convenience, the tabulated data are also presented in a graphical form (Fig. 12). The shaded region simply emphasizes the behavior with field size. Interestingly, the limited data, irrespective of the beam energy and the linac model, show remarkable agreement (maximum-to-minimum spread of ~2%). However, for field sizes smaller than 2×2 cm^2, the differences in S_c with respect to the model of the linac become significant (see Fig. 6). The dashed curve represents the RPC average of user submitted data, without any QA of the measured data. Strikingly, at photon energies exceeding 15 MV, the dashed curve

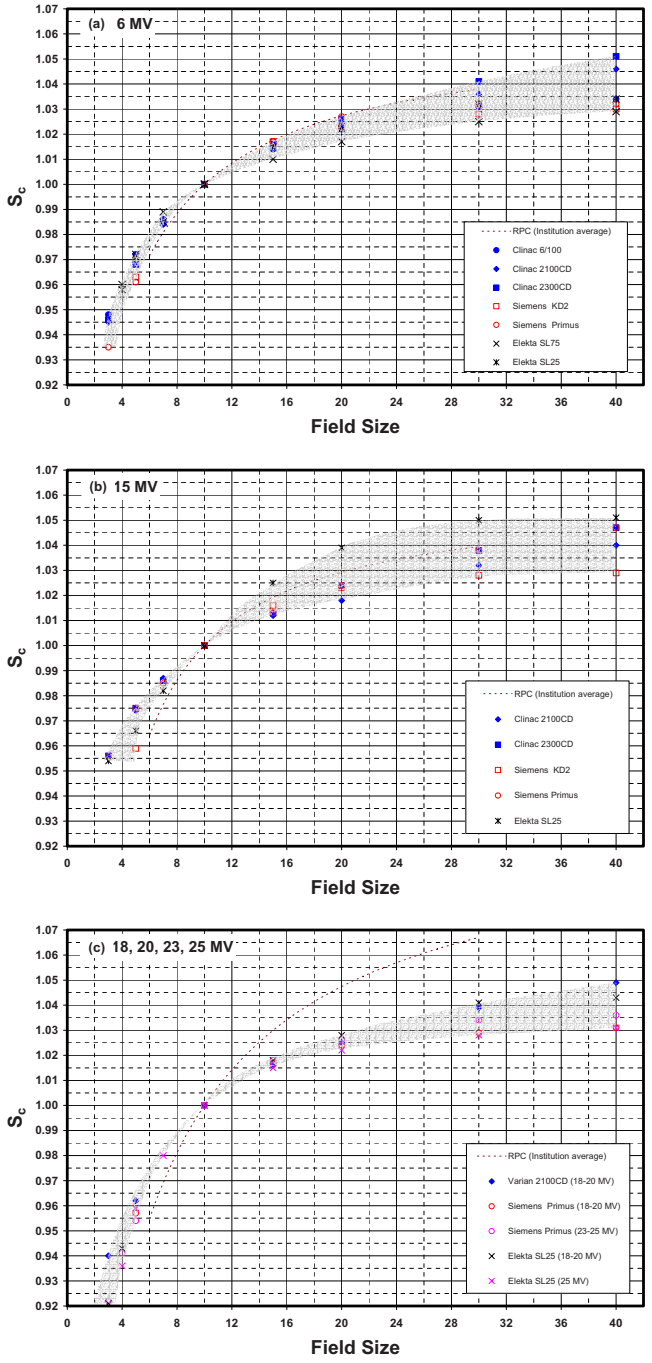

FIG. 12. Measured S_c for various accelerators for (a) 6 MV, (b) 15 MV, and (c) 18–25 MV. The symbols are measurement taken using the water-equivalent miniphantom described in this report. The dashed line is average data submitted by users to RPC. The shaded area represents the variation among various accelerators. The cause of large discrepancy between the curve and the shaded area is most likely electron contamination due to in appropriate build-up cap, especially at energies >15 MV.

exhibits a significant departure from the plotted data points. Most build-up caps in current use are near depth of d_{max} instead of 10 cm. Therefore, it is important that electron contamination be avoided by use of build-up cap of adequate dimensions and proper material. (Note that this difference does not necessarily reflect an error in dose calculation provided that the beam data are normalized at the same depth.

Since the electron contamination can be strongly depth dependent for depths less than the range of highest electron energies, these data show potential large errors for photon energies larger than 15 MV if the depth of normalization is not chosen to be beyond the range of electron contamination.)

One may fit the measured values to a model such as shown by Eq. (36) by determining the three parameters (a_1, a_2, and λ). Table II provides a cross-check of the published parameters for known linear accelerators.

It has been proposed that one can measure the in-water phantom scatter factor (S_{cp}) to determine S_c using a known phantom scatter factor (S_p) and the relationship $S_c = S_{cp}/S_p$.[137] The phantom scatter factor S_p at 10 cm has been shown to be a function of quality index and field size and is not sensitive to the make/model of the linear accelerators.[12,138] Using these published data, the user can even determine S_c for square fields directly. However, this method is dependent on the correct value of S_p and thus needs to be further refined to determine S_c at off-axis locations.

The importance of the materials and dimensions of the miniphantom used should not be underestimated. This implies acquiring proper miniphantoms for both large (≥4 cm) and small (< 4 cm) fields is important. The RPC's analysis of S_c data from ~90 institutions (Fig. 12) shows that even for the same linac make/model, the data have a large spread of up to 4% (max/min).

As recommended in TG40,[136] the periodic (yearly) spot checks of open square field S_c values should be performed. One should be able to reproduce the values within 1%. Spot checks of the physical or dynamic wedged fields may not be necessary if open-field checks show an acceptable agreement. Spot checks of the MLC rectangular-field data are recommended for field sizes of 3×40 and 40×3 cm^2.

VIII. SUMMARY

(1) In-air output ratio, S_c, is defined as the ratio of collision kerma to water per monitor unit at a point in free space for an arbitrary collimator setting to that for a reference collimator setting. This definition ensures that S_c describes the photon transport only. S_c is caused by three physical effects: Source obscuring, headscattering, and monitor backscattering. Interested readers can refer to Sec. IV for details.

(2) The in-air output ratio should be measured at the point of interest using a miniphantom with sufficient longitudinal and lateral thicknesses to eliminate electron contamination. The cross section of the miniphantom should be completely covered by the collimator setting of the field. Figure 9 provides recommended geometries for the miniphantoms for normal collimator settings. For small collimator settings, a brass miniphantom (Fig. 10) can be used for collimator setting as small as 1.5×1.5 cm^2. Section V C gives procedures for use of the high atomic number miniphantoms. For smaller field sizes, detailed recommendations of the miniphantom and detector combinations are included in Sec. V D.

(3) A correction-factor based formalism [Eq. (31)] is introduced to determine in-air output ratio measured using any geometries of miniphantom (or cap) composed of any material. This correction should be applied under conditions when a miniphantom of high-Z material with smaller longitudinal and/or lateral dimensions has to be used, e.g., for SRS fields and/or IMRT. Correction factors for common collimator settings can be found in literature.[14]

(4) Theoretical analysis is provided to determine the values of S_c and its components (headscatter, monitor backscattering) in clinical conditions different from that for rectangular fields [e.g., irregular (MLC) fields, wedge fields, and IMRT fields]. Headscatter at off-axis points are discussed. In addition, the concept of equivalent square for headscatter is introduced to determine S_c while accounting for the collimator exchange effect for various field shaping mechanisms (MLC replacing jaws, MLC as attachment, and/or blocks). Interested readers can refer to Sec. VI for details.

(5) A database of S_c for rectangular fields is provided for quality assurance of measured S_c. "QA" does not imply extensive repeated measurements of S_c but is a step (not necessarily measurement) to verify the measured values of S_c. Details are included in Sec. VII.

(6) S_c defined in this report can be used in meterset and dose calculation as described in Sec. III. It is suitable for TPR-based MU calculation algorithm where the reference depth is typically 10 cm or beyond electron contamination. However, this report does not provide a solution for situations when the historically used "collimator-scatter factor" measured at d_{max} is used for TMR-based MU calculation algorithm. In this case, TG74 recommend using S_c (in-air output ratio) as defined in this report so long as $S_p = S_{cp}/S_c$ is determined using S_{cp} measured at d_{max}.

ACKNOWLEDGMENTS

The authors thank Bengt E. Bjärngard for his valuable inputs and review of the document. We also thank the reviewers from AAPM Radiation Therapy Committee (RTC), John Gibbons, Dan Bourland, Marc Sontag, Ellen Yorke, X. Ronald Zhu, and Ying Xiao for their valuable inputs. We thank the referees for the Medical Physics Journal for the encouragement and many helpful critics.

APPENDIX A: MEASURED DATA FOR IN AIR OUTPUT RATIO FOR TYPICAL LINEAR ACCELERATORS

Measured in air output ratio are included for square open fields (Table III), square wedged fields (Table IV), and rectangular open fields (Table V).

TABLE III. Measured in-air output ratio versus square collimator settings for open fields. Data are compiled for comparison or quality assurance purpose only and are not to be used for clinical application. Measurement uncertainty is 0.5%.

Nom E (MV)	Collimator setting (cm)	Varian			Siemens		Elekta	
		6/100	2100CD	2300CD	KD2	Primus	SL75	SL25
6	3	0.948	0.945	0.946		0.935		
	4						0.960	0.958
	5	0.972	0.968	0.968	0.963	0.961	0.972	0.971
	7	0.986	0.984	0.985			0.989	0.985
	10	1.000	1.000	1.000	1.000	1.000	1.000	1.000
	15	1.014	1.016	1.016	1.017	1.017	1.010	1.015
	20	1.022	1.024	1.026	1.023	1.027	1.017	1.022
	30	1.031	1.036	1.041	1.028	1.032	1.025	1.032
	40	1.034	1.046	1.051	1.030	1.032	1.029	1.034
15	3		0.956	0.956		0.956		0.954
	4							
	5		0.974	0.975	0.959	0.975		0.966
	7		0.987	0.986		0.985		0.982
	10		1.000	1.000	1.000	1.000		1.000
	15		1.012	1.013	1.016	1.013		1.025
	20		1.018	1.024	1.023	1.024		1.039
	30		1.032	1.038	1.028	1.038		1.050
	40		1.040	1.047	1.029	1.047		1.051
18 or 20	3		0.940			0.919		0.921
	4							0.943
	5		0.962			0.957		0.959
	7							
	10		1.000			1.000		1.000
	15		1.016			1.017		1.018
	20		1.025			1.024		1.028
	30		1.039			1.029		1.041
	40		1.049			1.031		1.043
23 or 25	3					0.922		
	4					0.941		0.936
	5					0.954		0.959
	7							0.980
	10					1.000		1.000
	15					1.018		1.015
	20					1.026		1.022
	30					1.034		1.028
	40					1.036		1.031

TABLE IV. Measured in-air output ratio, $S_{c,w}$, versus square collimator settings for 60° wedged fields. Data are compiled for comparison or quality assurance purpose only and are not to be used for clinical use. Measurement uncertainty is 0.5%. (Note: $S_{c,w}$ should not be used simultaneously with field size dependent WF in MU calculation formalism.)

	Manufacturer			
c	Varian 2300CD		2100CD/MLC	
(cm)	6 MV	15 MV	6 MV	15 MV
3	0.935	0.943	0.920	0.928
5	0.959	0.965	0.945	0.951
7	0.978	0.980	0.970	0.972
10	1.000	1.000	1.000	1.000
15	1.029	1.026	1.042	1.038
15×20	1.040	1.038	1.058	1.054
15×30	1.057	1.055	1.081	1.077
15×40	1.069	1.064	1.095	1.090
	Elekta SL20		Elekta SL75	
	6 MV	25 MV	6 MV	
4	0.921	0.894	0.929	
5	0.940	0.933	0.946	
7	0.967	0.966	0.970	
10	1.000	1.000	1.000	
15	1.048	1.046	1.033	
20	1.074	1.072	1.058	
30	na	na	1.084	
	Siemens, KD2		Siemens, Primus	
	6 MV	15 MV	6 MV	18 MV
3	–	–	0.933	0.915
5	0.954	0.953	0.958	0.952
10	1.000	1.000	1.000	1.000
15	1.034	1.034	1.034	1.035
20	1.062	1.059	1.059	1.051
30	–	–	1.081	1.072

TABLE V. Measured in-air output ratio versus rectangular collimator settings for open fields of three major accelerator manufacturers (Elekta, Siemens, and Varian) for (a) 6 MV and (b) 15 (or 25) MV. *Y* is always upper collimator and *X* is always lower collimator. Measurement uncertainty is 0.5%.

(a)

Varian 2100C 6 MV							
Collimator setting ($X\backslash Y$)	4	7	10	15	20	30	40
4	0.953	0.963	0.968	0.970	0.970	0.971	0.971
7	0.968	0.983	0.989	0.991	0.992	0.994	0.996
10	0.975	0.994	1.000	1.005	1.006	1.007	1.008
15	0.982	1.002	1.012	1.017	1.018	1.020	1.021
20	0.987	1.008	1.017	1.022	1.024	1.028	1.028
30	0.992	1.014	1.024	1.031	1.033	1.038	1.037
40	0.997	1.019	1.030	1.036	1.041	1.045	1.044

Siemens Primus 6 MV							
Collimator setting ($X\backslash Y$)	3	5	10	15	20	30	40
3	0.935	0.942	0.950	0.952	0.953	0.956	0.957
5	0.952	0.961	0.972	0.975	0.976	0.976	0.976
10	0.966	0.982	1.000	1.005	1.006	1.010	1.010
15	0.971	0.989	1.011	1.017	1.020	1.022	1.022
20	0.973	0.993	1.017	1.024	1.027	1.030	1.031
30	0.976	0.997	1.019	1.026	1.029	1.032	1.032
40	0.976	0.997	1.021	1.029	1.031	1.033	1.032

Elekta SL25 6 MV								
Collimator setting ($X\backslash Y$)	3	5	10	15	20	25	30	40
3	0.955	0.962	0.970	0.972	0.975	0.975	0.974	0.969
5	0.964	0.977	0.988	0.992	0.990	0.994	0.989	0.992
10	0.975	0.987	1.000	1.009	1.012	1.013	1.013	1.012
15	0.980	0.992	1.011	1.017	1.021	1.023	1.023	1.021
20	0.981	0.995	1.014	1.020	1.026	1.028	1.026	1.025
25	0.981	0.996	1.016	1.023	1.028	1.028	1.030	1.026
30	0.982	0.997	1.018	1.024	1.030	1.032	1.031	1.021
40	0.986	0.998	1.018	1.025	1.032	1.032	1.031	1.026

(b)

Varian 2100C 15 MV							
Collimator setting ($X\backslash Y$)	4	7	10	15	20	30	40
4	0.958	0.966	0.970	0.971	0.972	0.973	0.974
7	0.972	0.984	0.989	0.992	0.994	0.994	0.995
10	0.980	0.994	1.000	1.004	1.006	1.007	1.008
15	0.985	1.002	1.009	1.015	1.017	1.019	1.019
20	0.990	1.007	1.015	1.021	1.024	1.028	1.027
30	0.996	1.015	1.024	1.031	1.035	1.039	1.039
40	1.001	1.021	1.030	1.038	1.042	1.045	1.046

Siemens Primus 15 MV							
Collimator setting ($X\backslash Y$)	3	5	10	15	20	30	40
3	0.919	0.933	0.938	0.942	0.943	0.941	0.943
5	0.944	0.957	0.970	0.971	0.975	0.977	0.978
10	0.961	0.983	1.000	1.007	1.006	1.010	1.010
15	0.966	0.990	1.011	1.017	1.021	1.022	1.024
20	0.969	0.992	1.017	1.024	1.024	1.027	1.030
30	0.969	0.991	1.016	1.025	1.028	1.029	1.034
40	0.971	0.996	1.021	1.023	1.026	1.029	1.031

TABLE V. (*Continued.*)

Collimator setting ($X\backslash Y$)	Elekta SL25 25 MV 3	5	10	15	20	25	30	40
3	0.923	0.936	0.946	0.947	0.947	0.949	0.951	0.951
5	0.942	0.961	0.976	0.979	0.979	0.980	0.983	0.985
10	0.957	0.979	1.000	1.006	1.008	1.010	1.014	1.015
15	0.961	0.984	1.009	1.015	1.019	1.021	1.024	1.025
20	0.962	0.985	1.013	1.018	1.022	1.025	1.028	1.030
25	0.963	0.986	1.014	1.019	1.025	1.028	1.031	1.030
30	0.963	0.987	1.015	1.021	1.026	1.029	1.033	1.033
40	0.964	0.987	1.016	1.021	1.027	1.032	1.034	1.033

APPENDIX B: DERIVATION OF MU FORMALISM FOR CONVENTIONAL METHOD

For the open beam, this alternative formulation for the dose at an arbitrary point can be derived as

$$
\begin{aligned}
D(c,s;x,y,z;d) &= \mathrm{MU}\frac{D_{\mathrm{ref}}}{\mathrm{MU}}\frac{\varepsilon(s;x,y,z;\overline{d})K_{\mathrm{inc}}(c;x,y,z)\mathrm{SF}(s;x,y,z;\overline{d})T(x,y;d)}{K_{\mathrm{inc}}(c_{\mathrm{ref}};x_{\mathrm{ref}},y_{\mathrm{ref}},z_{\mathrm{ref}})\mathrm{SF}(s_{\mathrm{ref}};x_{\mathrm{ref}},y_{\mathrm{ref}},z_{\mathrm{ref}};d_{\mathrm{ref}})T(x_{\mathrm{ref}},y_{\mathrm{ref}};d_{\mathrm{ref}})} = \mathrm{MU}\frac{D_{\mathrm{ref}}}{\mathrm{MU}} \\
&\times \frac{K_{\mathrm{inc}}(c;x_{\mathrm{ref}},y_{\mathrm{ref}},z_{\mathrm{ref}})}{K_{\mathrm{inc}}(c_{\mathrm{ref}};x_{\mathrm{ref}},y_{\mathrm{ref}},z_{\mathrm{ref}})}\frac{K_{\mathrm{inc}}(c;x,y,z_{\mathrm{ref}})T(x,y;d)}{K_{\mathrm{inc}}(c;x_{\mathrm{ref}},y_{\mathrm{ref}},z_{\mathrm{ref}})T(x_{\mathrm{ref}},y_{\mathrm{ref}};\overline{d})}\frac{K_{\mathrm{inc}}(c;x,y,z)}{K_{\mathrm{inc}}(c;x,y,z_{\mathrm{ref}})} \\
&\times \frac{\varepsilon(s;x,y,z;\overline{d})\mathrm{SF}(s;x,y,z;\overline{d})T(x_{\mathrm{ref}},y_{\mathrm{ref}};\overline{d})}{\mathrm{SF}(s_{\mathrm{ref}};x_{\mathrm{ref}},y_{\mathrm{ref}},z_{\mathrm{ref}};d_{\mathrm{ref}})T(x_{\mathrm{ref}},y_{\mathrm{ref}};d_{\mathrm{ref}})} \\
&= \mathrm{MU}\frac{D_{\mathrm{ref}}}{\mathrm{MU}}s_c(c)\cdot\mathrm{OAR}_{\mathrm{air}}(c;x,y;d)\cdot\mathrm{DIST}(c;x,y,z)\frac{\varepsilon(s;x,y,z;\overline{d})\mathrm{SF}(s;x,y,z;\overline{d})T(x_{\mathrm{ref}},y_{\mathrm{ref}};\overline{d})}{\mathrm{SF}(s_{\mathrm{ref}};x_{\mathrm{ref}},y_{\mathrm{ref}},z_{\mathrm{ref}};d_{\mathrm{ref}})T(x_{\mathrm{ref}},y_{\mathrm{ref}};d_{\mathrm{ref}})} \\
&= \mathrm{MU}\frac{D_{\mathrm{ref}}}{\mathrm{MU}}S_c(c)\cdot\mathrm{OAR}_{\mathrm{air}}(c;x,y;d)\cdot\mathrm{DIST}(c;x,y,z)\frac{\varepsilon(s';x_{\mathrm{ref}},y_{\mathrm{ref}},z_{\mathrm{ref}};\overline{d})\mathrm{SF}(s';x_{\mathrm{ref}},y_{\mathrm{ref}},z_{\mathrm{ref}};\overline{d})T(x_{\mathrm{ref}},y_{\mathrm{ref}};\overline{d})}{\mathrm{SF}(s_{\mathrm{ref}};x_{\mathrm{ref}},y_{\mathrm{ref}},z_{\mathrm{ref}};d_{\mathrm{ref}})T(x_{\mathrm{ref}},y_{\mathrm{ref}};d_{\mathrm{ref}})} \\
&= \mathrm{MU}\frac{D_{\mathrm{ref}}}{\mathrm{MU}}S_c(c)\mathrm{OAR}_{\mathrm{air}}(c;x,y;d)\cdot\mathrm{DIST}(c;x,y,z) \\
&\times \frac{\mathrm{SF}(s';x_{\mathrm{ref}},y_{\mathrm{ref}},z_{\mathrm{ref}};d_{\mathrm{ref}})}{\mathrm{SF}(s_{\mathrm{ref}};x_{\mathrm{ref}},y_{\mathrm{ref}},z_{\mathrm{ref}};d_{\mathrm{ref}})}\frac{\varepsilon(s';x_{\mathrm{ref}},y_{\mathrm{ref}},z_{\mathrm{ref}};\overline{d})\mathrm{SF}(s';x_{\mathrm{ref}},y_{\mathrm{ref}},z_{\mathrm{ref}};\overline{d})T(x_{\mathrm{ref}},y_{\mathrm{ref}};\overline{d})}{\mathrm{SF}(s';x_{\mathrm{ref}},y_{\mathrm{ref}},z_{\mathrm{ref}};d_{\mathrm{ref}})T(x_{\mathrm{ref}},y_{\mathrm{ref}};d_{\mathrm{ref}})} \\
&= \mathrm{MU}\frac{D_{\mathrm{ref}}}{\mathrm{MU}}S_c(c)\cdot\mathrm{OAR}_{\mathrm{air}}(c;x,y;d)\cdot\mathrm{DIST}(c;x,y,z)\cdot S_p(s')\cdot\mathrm{TPR}(s';\overline{d}) \\
&\approx \mathrm{MU}\frac{D_{\mathrm{ref}}}{\mathrm{MU}}S_c(c)\cdot S_p(s')\cdot\mathrm{TPR}(s';\overline{d})\cdot\mathrm{POAR}(x,y;d_{\mathrm{ref}})\cdot\mathrm{DIST}(z),
\end{aligned}
\tag{B1}
$$

where

$$
\mathrm{POAR}(x,y;d_{\mathrm{ref}}) = \frac{K_{\mathrm{inc}}(c_{\mathrm{max}};x,y,z_{\mathrm{ref}})T(x,y;d_{\mathrm{ref}})}{K_{\mathrm{inc}}(c_{\mathrm{max}};x_{\mathrm{ref}},y_{\mathrm{ref}},z_{\mathrm{ref}})T(x_{\mathrm{ref}},y_{\mathrm{ref}};\overline{d_{\mathrm{ref}}})} \tag{B2}
$$

and

$$
\mathrm{DIST}(z) = \frac{K_{\mathrm{inc}}(c_{\mathrm{ref}};x_{\mathrm{ref}},y_{\mathrm{ref}},z)}{K_{\mathrm{inc}}(c_{\mathrm{ref}};x_{\mathrm{ref}},y_{\mathrm{ref}},z_{\mathrm{ref}})} \tag{B3}
$$

Notice that the dosimetrical quantity, $D(c,s;x,y,z;d)$, implicitly includes the dependence on $\overline{d}$ since d changes with x, y and equals $\overline{d}$ on the central axis $(x_{\mathrm{ref}},y_{\mathrm{ref}})$. $\mathrm{TPR}(s';\overline{d})$, $S_p(s')$, and $S_c(c)$ are the central axis quantities for the open beam. The last line of Eq. (B1) becomes an approximation due to using the $\mathrm{POAR}(x,y;d_{\mathrm{ref}})$ instead of $\mathrm{OAR}_{\mathrm{air}}(c;x,y;d)$ (losing the dependence on c and d) using only the z dependence for distance function, and ignoring the off-axis change in the TPR.

From these equations, we get for the off-axis case with no wedge:

$$\mathrm{MU} = \frac{D(c,s;x,y,z;d)}{\frac{D_{\mathrm{ref}}}{\mathrm{MU}} \cdot S_{\mathrm{c}}(c) \cdot \mathrm{DIST}(z) \cdot \mathrm{POAR}(x,y;d_{\mathrm{ref}}) \cdot S_{\mathrm{p}}(s') \cdot \mathrm{TPR}(s';\overline{d})}. \tag{B4}$$

For the general case with a wedge, for any point in the patient,

$$\begin{aligned} D(c,s;x,y,z;d;w) &= D(c,s;x,y,z;d;o) \cdot \frac{D(c,s;x,y,z;d;w)}{D(c,s;x,y,s;d;o)} \\ &= \mathrm{MU} \cdot \frac{D_{\mathrm{ref}}}{\mathrm{MU}} \cdot S_{\mathrm{c}}(c) \cdot S_{\mathrm{p}}(s') \cdot \mathrm{TPR}(s';\overline{d}) \cdot \mathrm{DIST}(c;x,y,z) \cdot \mathrm{OAR}_{\mathrm{air}}(c;x,y;d) \cdot \mathrm{WF}(c,s;x,y,z;d;w) \\ &\approx \mathrm{MU}\frac{D_{\mathrm{ref}}}{\mathrm{MU}} \cdot S_{\mathrm{c}}(c) \cdot S_{\mathrm{p}}(s') \cdot \mathrm{TPR}(s';\overline{d}) \cdot \mathrm{DIST}(z) \cdot \mathrm{POAR}(x,y;d_{\mathrm{ref}}) \cdot \mathrm{WF}(c;x,y;d;w), \end{aligned} \tag{B5}$$

so that

$$\mathrm{MU} = \frac{D(c,s;x,y,z;d;w)}{\frac{D_{\mathrm{ref}}}{\mathrm{MU}} \cdot S_{\mathrm{c}}(c) \cdot S_{\mathrm{p}}(s') \cdot \mathrm{TPR}(s';\overline{d}) \cdot \mathrm{DIST}(z) \cdot \mathrm{POAR}(x,y;d_{\mathrm{ref}}) \cdot \mathrm{WF}(c;x,y;d;w)}. \tag{B6}$$

In Eq. (B6), the factors S_{c}, S_{p}, $\mathrm{TPR}(s';\overline{d})$, and $\mathrm{DIST}(z)$ represent the same functions used without a wedge. All of the wedge information becomes incorporated into the wedge factor $\mathrm{WF}(c;x,y;d;w)$, which varies with collimator setting, field size, distance from the source, and depth in the patient as well as the wedge angle.

[a]Electronic mail: tzhu@mail.med.upenn.edu

[1]A. Dutreix, B. E. Bjärngard, A. Bridier, B. Mijnheer, J. E. Shaw, and H. Svensson, *Monitor Unit Calculation For High Energy Photon Beams* (Garant Publishers, N. V., Leuven/Apeldoorn, 1997).

[2]M. E. J. Young, *Radiological Physics*, 1st ed. (Academic, New York, 1957).

[3]J. G. Holt, J. S. Laughlin, and J. P. Moroney, "The extension of the concept of tissue-air ratios (TAR) to high-energy x-ray beams," Radiology **96**, 437–446 (1970).

[4]S. Kim, J. R. Palta, and T. C. Zhu, "A generalized solution for the calculation of in-air output factors in irregular fields," Med. Phys. **25**, 1692–1701 (1998).

[5]F. Khan, *The Physics of Radiation Therapy*, 2nd ed. (Williams & Wilkins, Baltimore, MD, 1994).

[6]K. R. Kase and G. K. Svensson, "Head scatter data for several linear accelerators (4—18 MV)," Med. Phys. **13**, 530–532 (1986).

[7]M. Tatcher and B. E. Bjärngard, "Head-scatter factors and effective x-ray source positions in a 25-MV linear accelerator," Med. Phys. **19**, 685–686 (1992).

[8]T. C. Zhu and B. E. Bjärngard, "The fraction of photons undergoing head scatter in x-ray beams," Phys. Med. Biol. **40**, 1127–1134 (1995).

[9]D. A. Jaffray, J. J. Battista, A. Fenster, and P. Munro, "X-ray sources of medical linear accelerators: Focal and extra-focal radiation," Med. Phys. **20**, 1417–1427 (1993).

[10]M. B. Sharpe, D. A. Jaffray, J. J. Battista, and P. Munro, "Extrafocal radiation: A unified approach to the prediction of beam penumbra and output factors for megavoltage x-ray beams," Med. Phys. **22**, 2065–2074 (1995).

[11]T. C. Zhu and K. Manbeck, "CT reconstruction of x-ray source profile of a medical accelerator," Proc. SPIE **2132**, 242–253 (1994).

[12]J. J. M. van Gasteren, S. Heukelom, H. J. van Kleffens, R. van der Laarse, J. L. M. Venselaar, and C. F. Westerman, "The determination of phantom and collimator scatter components of the output of megavoltage photon beams: Measurement of the collimator scatter part with a beam-coaxial narrow cylindrical phantom," Radiother. Oncol. **20**, 250–257 (1991).

[13]M. R. Goede, D. W. Anderson, and K. L. McCray, "Corrections to megavoltage depth-dose values due to reduced backscatter thickness," Med. Phys. **4**, 123–128 (1977).

[14]J. Li and T. C. Zhu, "Measurement of in-air output ratios using different miniphantom materials," Phys. Med. Biol. **51**, 3819–3834 (2006).

[15]J. P. Gibbons, J. A. Antolak, D. S. Followill, M. S. Huq, E. E. Klein, K. L. Lam, J. R. Palta, D. M. Roback, and M. Reid, "Monitor unit calculations for external photon and electron beams: Report of the AAPM Radiation Therapy Committee Task Group No. 71," Med. Phys. (submitted).

[16]B. E. Bjärngard and H. Shackford, "Attenuation in high-energy x-ray beams," Med. Phys. **21**, 1069–1073 (1994).

[17]Y. Xiao, B. E. Bjarngard, and J. Reiff, "Equivalent fields and scatter integration for photon fields," Phys. Med. Biol. **44**, 1053–1065 (1999).

[18]R. C. Tailor, V. M. Tello, C. B. Schroy, M. Vossler, and W. F. Hanson, "A generic off-axis energy correction for linac beam dosimetry," Med. Phys. **25**, 662–667 (1998).

[19]A. Ahnesjö, "Analytic modeling of photon scatter from flattening filters in photon therapy beams," Med. Phys. **21**, 1227–1235 (1994).

[20]A. Ahnesjö, L. Weber, and P. Nilsson, "Modeling transmission and scatter for photon beam attenuators," Med. Phys. **22**, 1711–1720 (1995).

[21]M. Asell, "Development of optimized radiation therapy using external electron and photon beams," Ph.D. thesis University of Stockholm, 1999.

[22]T. R. Mackie, P. Reckwerdt, and N. Papanikolaou, in *3-D Radiation Treatment Planning and Conformal Therapy*, edited by J. A. Purdy and B. Emami (Medical Physics, Madison, WI, 1995).

[23]A. Ahnesjö, T. Knöös, and A. Montelius, "Application of the convolution method for calculation of output factors for therapy photon beams," Med. Phys. **19**, 295–304 (1992).

[24]B. Nilsson and A. Brahme, "Contamination of high-energy photon beams by scattered photons," Strahlentherapie **157**, 181–186 (1981).

[25]D. W. O. Rogers, B. A. Faddegon, G. X. Ding, C. M. Ma, J. We, and T. R. Mackie, "BEAM: A Monte Carlo code to simulate radiotherapy treatment units," Med. Phys. **22**, 503–524 (1995).

[26]B. Jiang, J. Deng, J. Li, T. Pawlicki, A. L. Boyer, and C.-M. Ma, *Modeling and Commissioning of Clinical Photon Beams for Monte Carlo Treatment Planning, Proc. of the XIII International Conference on the Use of Computer in Radiation Therapy (ICCR)*, edited by W. Schlegel and T. Bortfeld (Springer-Verlag, Heidelberg, 2000), pp. 434–436.

[27]C. M. Ma, J. S. Li, T. Pawlicki, S. B. Jiang, J. Deng, M. C. Lee, T. Koumrian, M. Luxton, and S. Brain, "A Monte Carlo dose calculation tool for radiotherapy treatment planning," Phys. Med. Biol. **47**, 1671–1689 (2002).

[28]S. Jiang, J. Deng, A. L. Boyer, and C. M. Ma, "An extrafocal source model for photon beam dose calculation," Med. Phys. **28**, 55–66 (2001).

[29]M. Fippel, F. Haryanto, O. Dohm, F. Nusslin, and S. Kriesen, "A virtual photon energy fluence model for Monte Carlo dose calculation," Med. Phys. **30**, 301–311 (2003).

[30]J. Deng, T. Guerrero, C.-M. Ma, and R. Nath, "Modelling 6 MV photon beams of a stereotactic radiosurgery system for Monte Carlo treatment planning," Phys. Med. Biol. **49**, 1689–1704 (2004).
[31]C. M. Ma, B. A. Faddegon, D. W. O. Rogers, and T. R. Mackie, "Accurate characterization of Monte Carlo calculated electron beams for radiotherapy," Med. Phys. **24**, 401–416 (1997).
[32]C.-M. Ma, "Characterization of computer simulated radiotherapy beams for Monte Carlo treatment planning," Radiat. Phys. Chem. **53**, 329–344 (1998).
[33]C.-M. Ma, E. Mok, A. Kapur, D. Findley, S. Brain, K. Forster, and A. L. Boyer, "Clinical implementation of a Monte Carlo treatment planning system," Med. Phys. **26**, 2133–2143 (1999).
[34]M. A. Ebert, P. Hoban, and P. J. Keall, "Modelling clinical accelerator beams: A review," Australas. Phys. Eng. Sci. Med. **19**, 131–150 (1996).
[35]A. Ahnesjö and M. M. Aspradakis, "Dose calculations for external photon beams in radiotherapy," Phys. Med. Biol. **44**, R99–R155 (1999).
[36]F. Verhaegen and J. P. Seuntjens, "Monte Carlo modelling of external radiotherapy photon beams," Phys. Med. Biol. **48**, R107–R164 (2003).
[37]I. J. Chetty, B. Curran, J. E. Cygler, J. J. DeMarco, G. Ezzell, B. A. Faddegon, I. Kawrakow, P. J. Keall, H. Liu, C. M. Ma, D. W. O. Rogers, J. Seuntjens, D. Sheikh-Bagheri, and J. V. Siebers, "Report of the AAPM Task Group No. 105: issues associated with clinical implementation of Monte Carlo-based photon and electron external beam treatment planning," Med. Phys. **34**, 4818–4853 (2007).
[38]R. Mohan, C. Chui, and L. Lidofsky, "Energy and angular distributions of photons from medical linear accelerators," Med. Phys. **12**, 592–597 (1985).
[39]D. Sheikh-Bagheri and D. W. O. Rogers, "Monte Carlo calculation of nine megavoltage photon beam spectra using the BEAM code," Med. Phys. **29**, 391–402 (2002).
[40]G. X. Ding, "Energy spectra, angular spread, fluence profiles and dose distributions of 6 and 18 MV photon beams: Results of Monte Carlo simulations for a Varian 2100EX accelerator," Med. Phys. **46**, 1025–1046 (2002).
[41]D. Sheikh-Bagheri and D. W. O. Rogers, "Sensitivity of megavoltage photon beam Monte Carlo simulations to electron beam and other parameters," Med. Phys. **29**, 379–390 (2002).
[42]A. Ahnesjo and P. Andreo, "Determination of effective bremsstrahlung spectra and electron contamination for photon dose calculations," Phys. Med. Biol. **34**, 1451–1464 (1989).
[43]O. Sauer and M. Neumann, "Reconstruction of high-energy bremsstrahlung spectra by numerical analysis of depth-dose data," Radiother. Oncol. **18**, 39–47 (1990).
[44]P. H. Huang, K. R. Kase, and B. E. Bjärngard, "Reconstruction of 4-MV bremsstrahlung spectra from measured transmission data," Med. Phys. **10**, 778–785 (1983).
[45]B. R. Archer, P. R. Almond, and L. K. Wagner, "Application of a Laplace transform pair modelfor high-energy x-ray spectral reconstruction," Med. Phys. **12**, 630–633 (1985).
[46]A. Piermattei, G. Arcovito, L. Azario, C. Bacci, L. Bianciardi, E. De Sapio, and C. Giacco, "A study of quality of bremsstrahlung spectra reconstructed from transmission measurements," Med. Phys. **17**, 227–233 (1990).
[47]C. R. Baker, B. Amaee, and N. M. Spyrou, "Reconstruction ofmegavoltage photon spectra by attenuation analysis," Phys. Med. Biol. **40**, 2041–2051 (1995).
[48]C. R. Baker and K. K. Peck, "Reconstruction of 6 MV photon spectra from measured transmission including maximum energy estimation," Phys. Med. Biol. **42**, 2041–2051 (1997).
[49]P. Francois, F. Coste, J. Bonnet, and O. Caselles, "Validation of reconstructed bremsstrahlung spectra between 6 MV and 25 MV from measured transmission data," Med. Phys. **24**, 769–773 (1997).
[50]A. Nisbet, H. Weatherburn, J. D. Fenwick, and G. McVey, "Spectral reconstruction of clinical megavoltage photon beams and the implications of spectral determination on the dosimetry of such beams," Phys. Med. Biol. **43**, 1507–1521 (1998).
[51]M. K. Yu, R. S. Sloboda, and B. Murray, "Linear accelerator photon beam quality at off-axis points," Med. Phys. **24**, 233–239 (1997).
[52]S. Zefkili, C. Kappas, and J. C. Rosenwald, "On-axis and off-axis primary dose component in high energy photon beams," Med. Phys. **21**, 799–808 (1994).
[53]H. Treuer, R. Boesecke, G. H. Hartmann, W. Schlegel, and W. J. Lorenz, "Dosimetrische Bestimmung der Primärfluenz und der Fokusgrösse eines 15-MeV-Linearbeschleunigers," in Medizinische Physik Vol. 87. DGMP und AGMP in Zusammenarbeit mit EFOMP. Hrsg. Helmar Bergmann. DGMP (1987), pp. 375–380.
[54]A. Ahnesjö and A. Trepp, "Acquisition of the effective lateral energy fluence distribution for photon beam dose calculations by convolution models," Phys. Med. Biol. **36**, 973–985 (1991).
[55]W. van der Zee and J. Welleweerd, "A Monte Carlo study on internal wedges using BEAM," Med. Phys. **29**, 876–885 (2002).
[56]F. Verhaegen and I. Das, "Monte Carlo modelling of a virtual wedge," Phys. Med. Biol. **44**, N251–259 (1999).
[57]R. Shih, X. A. Li, and J. C. H. Chu, "Dosimetric characteristics of dynamic wedged fields: A Monte Carlo study," Phys. Med. Biol. **46**, N281–292 (2001).
[58]R. Shih, X. A. Li, and J. C. H. Chu, "Dynamic wedge versus physical wedge: A Monte Carlo study," Med. Phys. **28**, 612–619 (2001).
[59]D. J. Dawson, "Percentage depth doses for high energy x-rays," Phys. Med. Biol. **21**, 226–235 (1976).
[60]M. S. Patterson and P. C. Shragge, "Characteristics of an 18 MV photon beam from a Therac 20 medical linear accelerator," Med. Phys. **8**, 312–318 (1981).
[61]G. Luxton and M. A. Astrahan, "Output factor constituents of a high-energy photon beam," Med. Phys. **15**, 88–91 (1988).
[62]Y. Yang, L. Xing, A. L. Boyer, Y. Song, and Y. Hu, "A three-source model for the calculation of head scatter factors," Med. Phys. **29**, 2024–2033 (2002).
[63]P. B. Dunscombe and J. M. Nieminen, "On the field-size dependence of relative output from a linear accelerator," Med. Phys. **19**, 1441–1444 (1992).
[64]X. R. Zhu and M. T. Gillin, "Derivation of the distribution of extrafocal radiation for head scatter factor calculation," Med. Phys. **32**, 351–359 (2005).
[65]E. L. Chaney, T. J. Cullip, and T. A. Gabriel, "A Monte Carlo study of accelerator head scatter," Med. Phys. **21**, 1383–1390 (1994).
[66]G. X. Ding, "An investigation of accelerator head scatter and output factor in air," Med. Phys. **31**, 2527–2533 (2004).
[67]A. R. Hounsell and J. M. Wilkinson, "Tissue standard ratios for irregularly shaped radiotherapy fields," BJR Suppl. **63**, 629–634 (1990).
[68]T. C. Zhu, B. E. Bjärngard, Y. Xiao, and M. Bieda, "Output ratio in air for MLC shaped irregular fields," Med. Phys. **31**, 2480–2490 (2004).
[69]H. H. Liu, T. R. Mackie, and E. C. McCullough, "A dual source photon beam model used in convolution/superposition dose calculations for clinical megavoltage x-ray beams," Med. Phys. **24**, 1960–1974 (1997).
[70]T. C. Zhu and B. E. Bjarngard, "Head-scatter off-axis for megavoltage x-rays," Med. Phys. **30**, 533–543 (2003).
[71]R. Shih, X. A. Li, J. C. H. Chu, and W. L. Hsu, "Calculation of head-scatter factors at isocenter or at center of field for any arbitrary jaw setting," Med. Phys. **26**, 506–511 (1999).
[72]A. P. Butler and J. P. Turner, "Off-axis output factors for 6 MV and 18 MV photons," Australas. Phys. Eng. Sci. Med. **20**, 177–182 (1997).
[73]A. L. McKenzie and P. H. Stevens, "How is photon head scatter in a linear accelerator related to the concept of a virtual source?," Phys. Med. Biol. **38**, 1173–1180 (1993).
[74]S. Kim, C. R. Liu, C. Chen, and J. R. Palta, "Two-effective-source method for the calculation of in-air output at various source-to-detector distances in wedge fields," Med. Phys. **26**, 949–955 (1999).
[75]T. C. Zhu, B. E. Bjarngard, and P. Vadash, "Scattered photon from wedges in high-energy x-ray beams," Med. Phys. **22**, 1339–1342 (1995).
[76]M. K. Islam and J. Van Dyk, "Effects of scatter generated by beam-modifying absorbers in megavoltage photon beams," Med. Phys. **22**, 2075–2081 (1995).
[77]H. H. Liu, T. R. Mackie, and E. C. McCullough, "Correcting kernel tilting and hardening in convolution/superposition dose calculations for clinical divergent and polychromatic photon beams," Med. Phys. **24**, 1729–1741 (1997).
[78]A. E. Schach von Wittenau, P. M. J. Bergstrom, and L. Cox, "Patient-dependent beam-modifier physics in Monte Carlo photon dose calculations," Med. Phys. **27**, 935–947 (2000).
[79]K. de Vlamynck, H. Palmans, F. Verhaegen, C. de Wagter, W. de Neve, and H. Thierens, "Dose measurements compared with Monte Carlo simulations of narrow 6 MV multileaf collimator shaped pphoton beams," Med. Phys. **26**, 1874–1882 (1999).
[80]J. Deng, S. B. Jiang, J. S. Li, T. Pawlicki, and C.-M. Ma, "Photon beam characterization and modeling for Monte Carlo treatment planning,"

Phys. Med. Biol. **45**, 411–427 (2000).
[81]H. Palmans, F. Verhaegen, F. Buffa, and C. Mubata, *Considerations for modeling MLCs with Monte Carlo techniques, Proc. of the XIII International Conference on the Use of Computer in Radiation Therapy (ICCR)*, edited by W. Schlegel and T. Bortfeld (Springer-Verlag, Heidelberg, 2000), pp. 458–460.
[82]A. Ahnesjö, "Collimator scatter in photon therapy beams," Med. Phys. **22**, 267–278 (1995).
[83]M. R. Arnfield, J. V. Siebers, J. O. Kim, Q. Wu, P. J. Keall, and R. Mohan, "A method for determining multileaf collimator transmission and scatter for dynamic intensity modulated radiotherapy," Med. Phys. **27**, 2231–2241 (2000).
[84]J. van der Walle, C. Martens, N. Reynaert, H. Palmans, M. Coghe, W. de Neve, C. de Wagter, and H. Thierens, "Monte Carlo model of the Elekta SLiplus accelerator: Validation of a new MLC component module in BEAM for a 6 MV beam," Phys. Med. Biol. **48**, 371–385 (2003).
[85]J. Deng, T. Pawlicki, Y. Chen, J. Li, S. B. Jiang, and C. M. Ma, "The MLC tongue-and-groove effect on IMRT dose distributions," Phys. Med. Biol. **46**, 1039–1060 (2001).
[86]M. Thatcher and B. E. Bjärngard, "Head-scatter factors in blocked photon fields," Radiother. Oncol. **33**, 64–67 (1994).
[87]P. A. Jursinic, "Changes in incident photon fluence of 6 and 18 MV x rays caused by blocks and block trays," Med. Phys. **26**, 2092–2098 (1999).
[88]J. van Dam, A. Bridier, C. Lasselin, N. Blanckaert, and A. Dutreix, "Influence of shielding blocks on the output of photon beams as a function of energy and type of treatment unit," Radiother. Oncol. **24**, 55–59 (1992).
[89]P. D. Higgins, D. N. Mihailidis, F. M. Kahn, E. J. Lee, and A. S. Ahuja, "Blocked field effects on collimator scatter factors," Phys. Med. Biol. **42**, 2435–2447 (1997).
[90]H. Kubo, "Telescopic measurements of backscattered radiation from secondary collimator jaws to a beam monitor chamber using a pair of slits," Med. Phys. **16**, 295–298 (1989).
[91]C. Duzenli, B. McClean, and C. Field, "Backscatter into the beam monitor chamber: Implications for dosimetry of asymmetric collimators," Med. Phys. **20**, 363–367 (1993).
[92]K. L. Lam, M. S. Muthuswamy, and R. K. Ten Haken, "Measurement of backscatter to the monitor chamber of medical accelerators using target charge," Med. Phys. **25**, 334–338 (1998).
[93]M. K. Yu, R. S. Sloboda, and F. Mansour, "Measurement of photon beam backscatter from collimators to the beam monitor chamber using target-current-pulse-counting and telescope techniques," Phys. Med. Biol. **41**, 1107–1117 (1996).
[94]P. H. Huang, J. Chu, and B. E. Bjärngard, "The effect of collimator-backscatter radiation on photon output of linear accelerators," Med. Phys. **14**, 268–269 (1987).
[95]D. L. Watts and G. S. Ibbott, "Measurement of beam current and evaluation of scatter production in an 18-MV accelerator," Med. Phys. **14**, 662–664 (1987).
[96]A. R. Hounsell, "Monitor chamber backscatter for intensity modulated radiation therapy using multileaf collimators," Phys. Med. Biol. **43**, 445–454 (1998).
[97]H. H. Liu, T. R. Mackie, and E. C. McCullough, "Calculating output factors for photon beam radiotherapy using a convolution/superposition method based on a dual source photon beam model," Med. Phys. **24**, 1975–1985 (1997).
[98]X. R. Zhu, Y. Kang, and M. Gillin, "Measurements of in-air output ratios for a linear accelerator with and without the flattening filter," Med. Phys. **33**, 3723–3733 (2006).
[99]F. Verhaegen, R. S. Tayler, H. H. Liu, and A. E. Nahum, "Backscatter towards the monitor ion chamber in high-energy photon and electron beams: Charge integration versus Monte Carlo simulation," Phys. Med. Biol. **45**, 3159–3170 (2000).
[100]T. C. Zhu and B. E. Bjarngard, "The head-scatter factor for small field sizes," Med. Phys. **21**, 65–68 (1994).
[101]S. Gotoh, M. Ochi, N. Hayashi, S. Matsushima, T. Uchida, S. Obata, K. Minami, K. Hayashi, T. Matsuo, M. Iwanaga, A. Yasunaga, and S. Shibata, "Narrow photon beam dosimetry for linear accelerator radiosurgery," Radiother. Oncol. **41**, 221–224 (1996).
[102]T. C. Zhu, B. E. Bjärngard, and H. Shackford, "X-ray source and the output factor," Med. Phys. **22**, 793–798 (1995).
[103]B. R. Thomadsen, S. Kubsad, B. R. Paliwal, S. Shahabi, and T. R. Mackie, "On the cause of the variation in tissu-maximum ratio values with source-to-detector distance," Med. Phys. **20**, 723–727 (1993).
[104]D. M. Frye, B. R. Paliwal, B. R. Thomadsen, and P. Jursinic, "Intercomparison of normalized head-scatter factor measurement techniques," Med. Phys. **22**, 249–253 (1995).
[105]J. Venselarr, S. Heukelom, N. Jager, B. Mijnheer, R. van der Laarse, H. van Gasteren, H. J. van Kleffens, and C. F. Westerman, "Effect of electron contamination on scatter correction factors for photon beam dosimetry," Med. Phys. **26**, 2099–2106 (1999).
[106]J. Spicka, D. Herron, and C. Orton, "Separating output factor into collimator factor and phantom scatter factor for megavoltage photon calculations," Med. Dosim. **13**, 23–24 (1988).
[107]P. Jursinic and B. R. Thomadsen, "Measurements of head-scatter factors with cylindrical build-up caps and columnar miniphantoms," Med. Phys. **26**, 512–517 (1999).
[108]L. Weber, P. Nilsson, and A. Ahnesjö, "Build-up cap materials for measurement of photon head-scatter factors," Phys. Med. Biol. **42**, 1875–1886 (1997).
[109]R. K. Ten Haken, "Comment on "Intercomparison on normalized head-scatter factor measurement techniques"," Med. Phys. **22**, 1471–1475 (1995).
[110]X. A. Li, M. Soubra, J. Szanto, and L. H. Gerig, "Lateral electron equilibrium and electron contamination in measurements of head-scatter factors using miniphantoms and brass caps," Med. Phys. **22**, 1167–1170 (1995).
[111]S. Johnsson, C. Ceberg, T. Knöös, and P. Nilsson, "Transmission measurements in air using the ESTRO mini-phantom," Phys. Med. Biol. **44**, 2445–2450 (1999).
[112]E. Tonkopi, M. R. EcEwen, B. R. Walters, and I. Kawrakow, "Influence of ion chamber response on in-air profile measurements in megavoltage photon beams," Med. Phys. **32**, 2918–2927 (2005).
[113]M. G. Karlsson, M. Karlsson, R. Sjogren, and H. Svensson, "Semiconductor detectors in output factor measurements," Radiother. Oncol. **42**, 293–296 (1997).
[114]C. McKerracher and D. I. Thwaites, "Headscatter factors for small MV photon fields. Part II: the effects of source size and detector," Radiother. Oncol. **85**, 286–291 (2007).
[115]P. A. Jursinic, "Measurement of head scatter factors of linear accelerators with columnar miniphantoms," Med. Phys. **33**, 1720–1728 (2006).
[116]K. Eklund and A. Ahnesjo, "Fast modeling of spectra and stopping-power ratios using differentiated fluence pencil kernels," Phys. Med. Biol. **59**, 4231–4247 (2008).
[117]W. A. Tome and J. R. Palta, "On the calculation of mean restricted collision stopping powers," Med. Phys. **25**, 758–772 (1998).
[118]S. Heukelom, J. H. Lanson, and B. J. Mijnheer, "Differences in wedge factor determination in air using a PMMA mini-phantom or a brass build-up cap," Med. Phys. **24**, 1986–1991 (1997).
[119]C. McKerracher and D. I. Thawaites, "Head scatter factors for small MV photon fields. Part I: a comparison of phantom types and methodologies," Radiother. Oncol. **85**, 277–285 (2007).
[120]M. Tatcher and B. E. Bjärngard, "Head-scatter factors in rectangular fields," Med. Phys. **20**, 205–206 (1993).
[121]P. Vadash and B. E. Bjärngard, "An equivalent-square formula for head-scatter factors," Med. Phys. **20**, 733–734 (1993).
[122]S. Kim, T. C. Zhu, and J. R. Palta, "An equivalent square formula for determining head scatter factors," Med. Phys. **24**, 1770–1774 (1997).
[123]T. C. Zhu, B. E. Bjärngard, Y. Xiao, and Y. Yang, "Modeling the output ratio in air for megavoltage photon beams," Med. Phys. **28**, 925–937 (2001).
[124]M. K. Yu, B. Murray, and R. Slobda, "Parameterization of head-scatter factors for rectangular photon fields using an equivalent square formalism," Med. Phys. **22**, 1329–1332 (1995).
[125]J. R. Palta, D. K. Yeung, and V. Frouhar, "Dosimetric considerations for a multileaf conllimator system," Med. Phys. **23**, 1219–1224 (1996).
[126]M. J. Day and G. A. Aird, "The equivalent-field method for dose determinations in rectangular fields," Br. J. Radiol., Suppl. **17**, 105–114 (1983).
[127]J. Clarkson, "A note on depth dose in fields of irregular shape," Br. J. Radiol. **14**, 265–268 (1941).
[128]A. L. Boyer, T. G. Ochran, C. E. Nyerick, T. J. Waldron, and C. J. Huntzinger, "Clinical dosimetry for implementation of a multileaf collimator," Med. Phys. **19**, 1255–1261 (1992).
[129]C. R. Liu, T. C. Zhu, and J. R. Palta, "Characterizing output for dynamic wedges," Med. Phys. **23**, 1213–1218 (1996).
[130]C. Liu, Z. Li, and J. R. Palta, "Characterizing output for the Varian en-

hanced dynamic wedge field," Med. Phys. **25**, 64–70 (1998).
[131]M. B. Sharpe, B. M. Miller, D. Yan, and J. W. Wong, "Monitor unit settings for intensity modulated beams delivered using a step-and-shoot approach," Med. Phys. **27**, 2719–2725 (2000).
[132]A. R. Hounsell and J. M. Wilkinson, "Head scatter modelling for irregular field shaping and beam intensity modulation," Phys. Med. Biol. **42**, 1737–1749 (1997).
[133]Y. Yang, L. Xing, J. S. Li, J. R. Palta, C. Chen, G. Luxton, and A. L. Boyer, "Independent dosimetric calculation with inclusion of head scatter and MLC transmission for IMRT," Med. Phys. **30**, 2937–2947 (2003).
[134]S. A. Naqvi, M. Sarfaraz, C. Holmes, X. Yu, and X. A. Li, "Analysing collimator structure effects in head-scatter calculations for IMRT class fields using scatter raytracing," Phys. Med. Biol. **46**, 2009–2028 (2001).
[135]A. R. Hounsell and J. M. Wilkinson, "Head scatter modelling for conformal radiotherapy and intensity modulated beams," in Proc. 12th Int. Conf. on the Use of Computers in Radiation Therapy, edited by D. D. Leavitt and G. Starkschall (Medical Physics Publishing, Salt Lake City, UT, 1997), pp. 216–218.
[136]G. J. Kutcher, L. Coia, M. Gillin, W. F. Hanson, S. Leibel, R. J. Morton, J. R. Palta, J. A. Purdy, L. E. Reinstein, G. K. Svensson, M. Weller, and L. Wingfield, "Comprehensive QA for radiation oncology: Report of AAPM Radiation Therapy Committee Task Group 40," Med. Phys. **21**, 581–618 (1994).
[137]K. L. Lam and R. K. Ten Haken, "In phantom determination of collimator scatter factor," Med. Phys. **23**, 1207–1212 (1996).
[138]T. Nyholm, J. Olofsson, A. Ahnesjö, and K. M., "Photon pencil kernel parameterisation based on beam quality index," Radiother. Oncol. **78**, 347–351 (2006).